iScience

CellPress
OPEN ACCESS

Article

# Restriction of Conformation Transformation in Excited State: An Aggregation-Induced Emission Building Block Based on Stable Exocyclic C=N Group

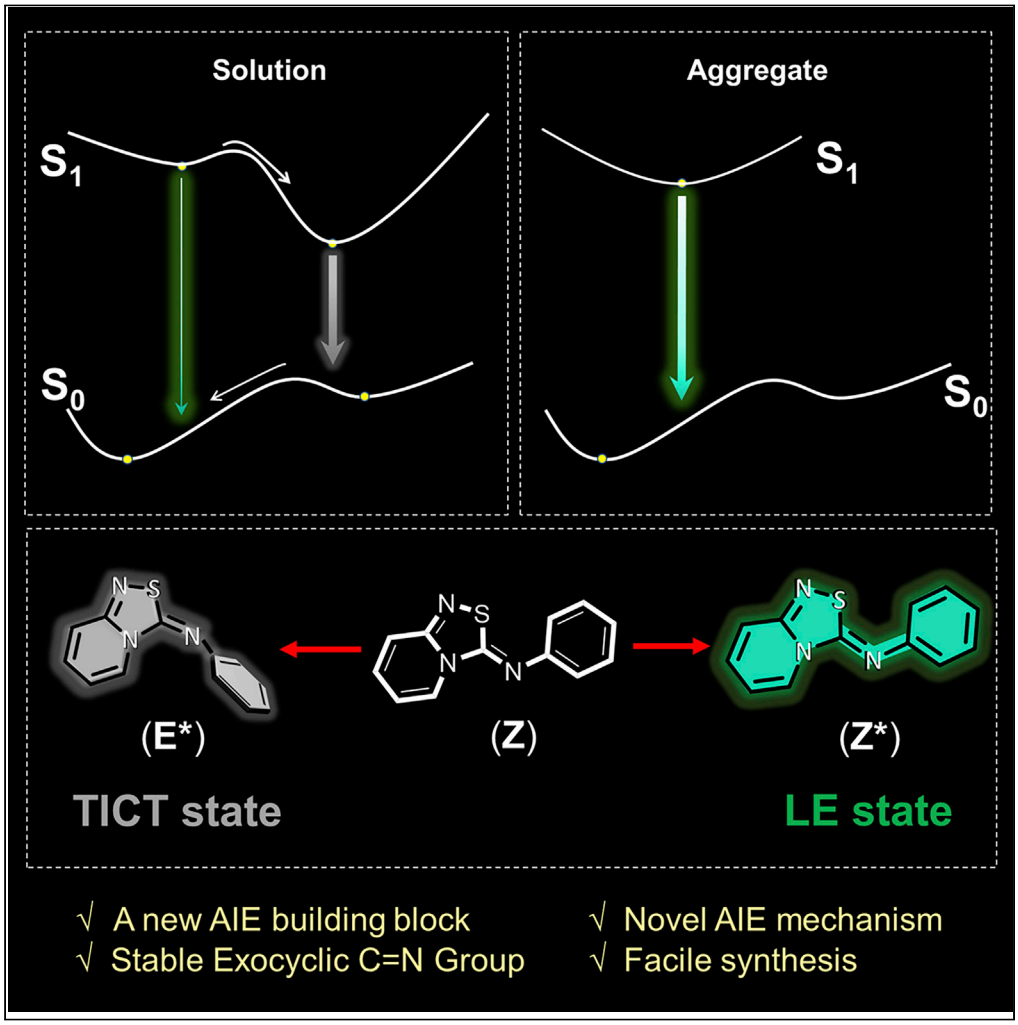


Wentao Yu, Han Zhang, Ping-An Yin, ..., Qian Peng, Huanfeng Jiang, Ben Zhong Tang

wangzhiming@scut.edu.cn (Z.W.)
cewuwq@scut.edu.cn (W.W.)
qpeng@iccas.ac.cn (Q.P.)
jianghf@scut.edu.cn (H.J.)
tangbenz@ust.hk (B.Z.T.)

## HIGHLIGHTS

A new aggregation-induced emission building block

A novel AIE mechanism with spectral measurements and theoretical calculations

Available starting materials resulting in convenient synthesis and modification

A stable exocyclic C=N double bond in heterocycles

Yu et al., iScience *23*, 101587
October 23, 2020 
https://doi.org/10.1016/j.isci.2020.101587

iScience

CellPress
OPEN ACCESS

Article

# Restriction of Conformation Transformation in Excited State: An Aggregation-Induced Emission Building Block Based on Stable Exocyclic C=N Group

Wentao Yu,[1,5] Han Zhang,[2,5] Ping-An Yin,[2,5] Fan Zhou,[2] Zhiming Wang,[2,6,*] Wanqing Wu,[1,*] Qian Peng,[3,*] Huanfeng Jiang,[1,*] and Ben Zhong Tang[2,4,*]

## SUMMARY

**The development of aggregation-induced emission (AIE) building block and deciphering its luminescence mechanism are of great significance. Here a feasible strategy for the construction of AIE unit based on *E-Z* isomerization (EZI) of exocyclic C=N double bond is proposed. Taking [1,2,4]thiadiazole[4,3-*a*]pyridine (TZP) derivative as an example, its aryl-substituted derivative (TZPP) shows obvious AIE character. The analysis of spectral data and theoretical calculations indicates that fast structural relaxation of TZPP in the emissive state plays a key role in a low fluorescence quantum yield in dilute solution, which should be caused by the small energy gap between locally excited (LE) state and twisted intramolecular charge transfer state. When in solid state, the bright emission with LE state characteristic reappears due to the large shift barrier of geometry transformation. As a potential building block for AIEgens with special heterocyclic structure, these findings would open up opportunities for developing various functional materials.**

## INTRODUCTION

Aggregation-induced emission (AIE) (Luo et al., 2001; Mei et al., 2015), a novel photo-physics concept, has led to great interest in the past two decades. Generally, the luminogens with AIE characteristic (AIEgens) are weak fluorescent or non-fluorescent in solution state, but emit intense fluorescence when they aggregate in solid state, which is different from the traditional organic emitters with excellent photoluminescence (PL) performance in dispersive state rather than in aggregates. Based on these remarkable advantages, AIEgens are widely applied to various fields depending on aggregate luminescence, such as organic light-emitting diodes (OLEDs) and organic nano-dots for bio-imaging (Wei et al., 2018a; Hu et al., 2018; Feng and Liu, 2018; Kwok et al., 2015; Zhang et al., 2019; Qian and Tang, 2017).

Recently, many great efforts have been made to explore deeply AIE working processes as well as their mechanisms, so that a large number of material systems have been enriched following these rules by chemists (Chen et al., 2019; Kokado et al., 2019; Gon et al., 2018; Sasaki et al., 2016; Tu et al., 2019; Zhou et al., 2019; Wang et al., 2018; He et al., 2019). Tetraphenylethylene (TPE), as a star building block in AIE family is studied and applied widely (Feng et al., 2018; Lu et al., 2019; Wang et al., 2019a). It is currently believed that the free rotation restriction of the double bond at the excited state is the key factor for AIE activity besides restricted rotation of the phenyl group (Scheme 1A) (Kokado et al., 2018; Cai et al., 2018). In solution state, the central olefinic double bond of TPE unit will be opened and two diphenylmethylene (DPM) units are generated in the excited state. The rotations, twisting motions, and inter-frictions between each other or solvent media of DPM moieties would dissipate the excited state energy, which would compete with the radiation transition process (Shustova et al., 2012; Sturala et al., 2017; Zhang et al., 2017). Thus, the *E-Z* isomerization (EZI) in the central double bond has a critical contribution in the emission quenching (Xie and Li, 2019; Xiong et al., 2018; Tseng et al., 2012; Wei et al., 2018b; Zhang et al., 2014). However, when the EZI process is restricted, the bright emission reappears in solid state. In fact, when a large steric group is introduced or the rigid cycle between two phenyl groups in DPM is formed, the conversion between *E*- and *Z*-isomers would be largely blocked, and the AIE phenomenon becomes less obvious. Employing systematic photophysical studies and simulation calculation, this limited photo-switches process is confirmed. According to this theory, there should be enhanced effect on EZI process if the peripheral

[1]Key Laboratory of Functional Molecular Engineering of Guangdong Province, School of Chemistry and Chemical Engineering, South China University of Technology (SCUT), Guangzhou 510640, China

[2]AIE Institute, SCUT-HKUST Joint Research Institute, Guangzhou International Campus, State Key Laboratory of Luminescent Materials and Devices, South China University of Technology, Guangzhou 510640, China

[3]Key Laboratory of Organic Solids, Beijing National Laboratory for Molecular Science, Institute of Chemistry, Chinese Academy of Sciences, Beijing 100190, China

[4]Department of Chemistry, Hong Kong Branch of Chinese National Engineering Research Center for Tissue Restoration and Reconstruction, The Hong Kong University of Science and Technology (HKUST), Clear Water Bay, Kowloon, Hong Kong, China

[5]These authors contributed equally

[6]Lead Contact

*Correspondence: wangzhiming@scut.edu.cn (Z.W.), cewuwq@scut.edu.cn (W.W.), qpeng@iccas.ac.cn (Q.P.), jianghf@scut.edu.cn (H.J.), tangbenz@ust.hk (B.Z.T.)

https://doi.org/10.1016/j.isci.2020.101587

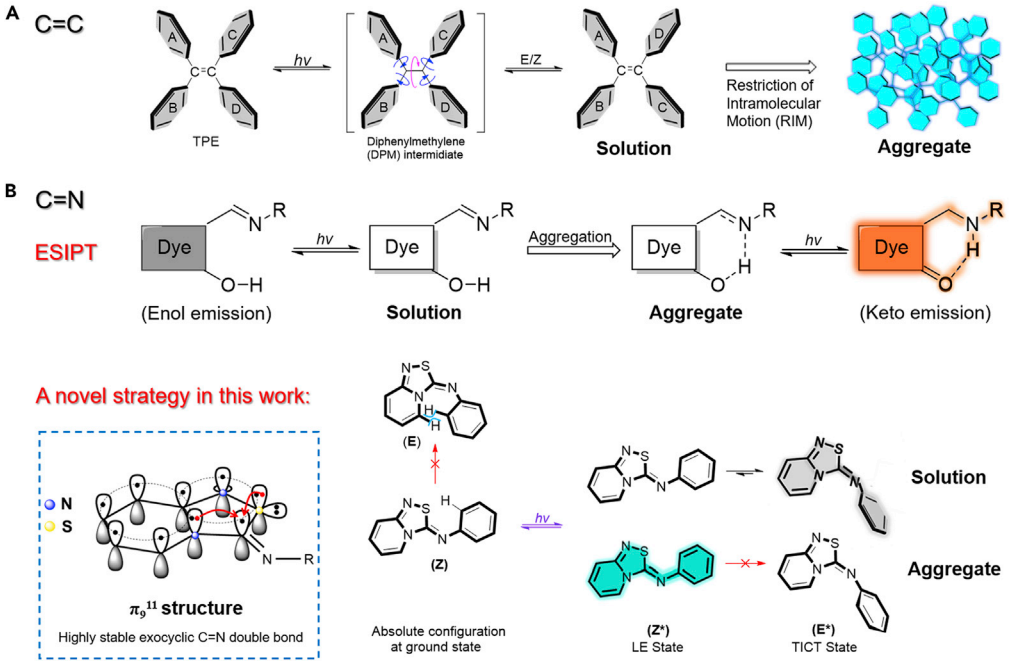


**Scheme 1. The Development of AIE Based on Double Dound**

(A) AIE mechanism of TPE based on C=C double bond.

(B) Two construction strategies (ESIPT/exocyclic) for AIE formation based on the C=N double bond.

substituted groups become small enough, and a better AIE-active building block would be possibly obtained.

As we known, the lone pair electrons (LPEs) are considered as the smallest substitution group, so that it is even possible to achieve "turn-off" luminescence output when the C=C double bond is replaced by the C=N double bond in solution. While in solid, this switch process as described above would be blocked, and the strong emission would reappear. Standing point of view, this kind of C=N double bond is indeed an ideal model to form the ideal AIEgens' building block. However, the C=N double bond in non-cyclic structure is a relatively unstable unit, leading to difficulty in expanding its functional applications due to the sensitivity to acid, base, and water. In addition, this EZI process between LPEs and another substituent attached to the *N* atom is sometimes difficult to be suppressed in aggregates, leading to an AIE effect not as good as expected (Belowicha and Stoddart, 2012). A general strategy for inhibiting these solid motions is to insert an *ortho*-hydroxyl group at the adjacent position of the C=N group, and the generated intramolecular hydrogen bonding via the formation of five- or six-membered heterocyclic intermediates would stabilize the C=N group to some degree. So, a series of AIEgens based on excited state intramolecular proton transfer (ESIPT) process (Tong et al., 2017; Zhang et al., 2015; Suzuki et al., 2014; Tseng et al., 2016; Wang et al., 2019b; Berenbeim et al., 2019) have been developed and applied in organic materials and bioactive compounds, such as carrier transport materials in OLEDs and biological active materials (Scheme 1B) (Sedgwick et al., 2018; Zhou et al., 2018; Padalkar et al., 2016).

In this contribution, a feasible strategy for constructing a stable AIEgens' building block is attempted based on [1,2,4]thiadiazole[4,3-*a*]pyridine (TZP) unit, which is developed in our group as a new-born heterocycle unit with special exocyclic C=N double bond (Yu et al., 2018b; Tang et al., 2018). On the one hand, in its main molecular conjugated $\pi$-system, 11 $\pi$-electrons are shared by 9 atoms to form $\pi_9^{11}$ electron-rich structure, which would increase the electron cloud density of the carbon atom in the C=N group and thus reduce its chance of being attacked by nucleophiles, and the stability of C=N group would be improved. On the other hand, the repulsive force on the hydrogen-hydrogen atom between the TZP ring and the substituent on C=N moieties could provide certain locking capabilities, and result in the *Z*-conformation at ground state. In addition, owing to the intermolecular interactions, the EZI process of C=N moiety may be further restricted in aggregates, which is conductive to the AIE behavior. So, this

CellPress
OPEN ACCESS

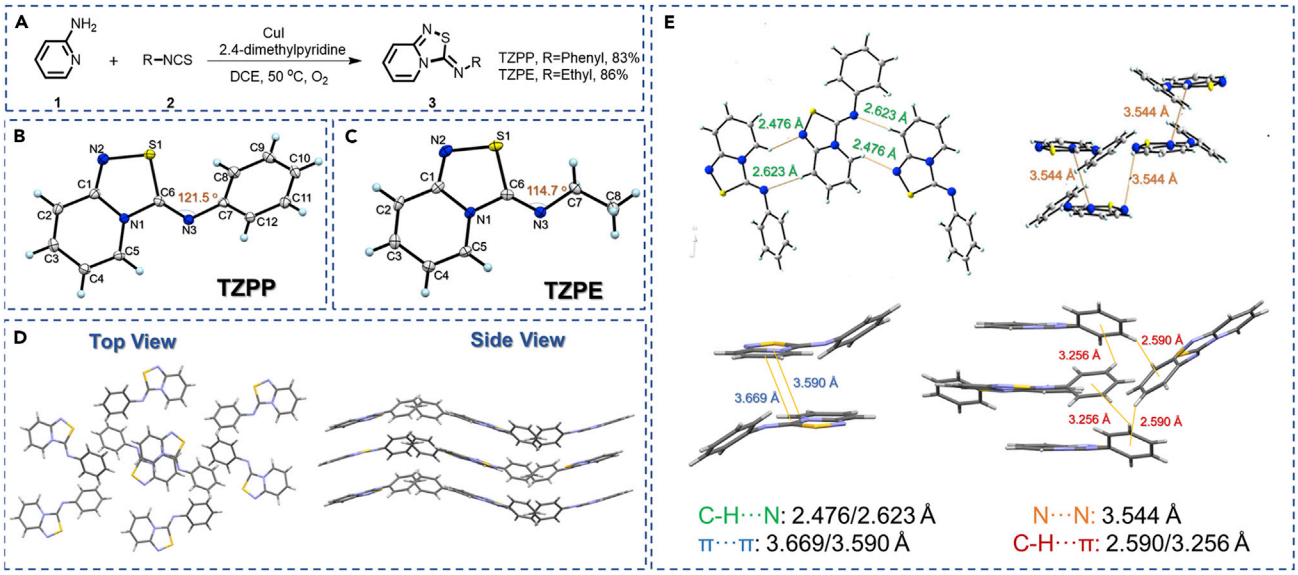


**Scheme 2. Synthesis and Characteristic of TZPP and TZPE**

(A) Synthetic routes of TZPP and TZPE.

(B and C) Crystal structures of TZPP and TZPE with the thermal ellipsoids set at 50% probability, respectively.

(D and E) Packing pattern of TZPP in crystals.

re-modification for TZP is meaningful to obtain AIE building block. After one-pot protocol, (*Z*)-*N*-phenyl-3*H*-[1,2,4]thiadiazolo[4,3-*a*]pyridine-3-imine (TZPP) and (*Z*)-*N*-ethyl-3*H*-[1,2,4]thiadiazolo[4,3-*a*]pyridin-3-imine (TZPE) are constructed efficiently to discuss the aryl or alkyl group substitution effect on their respective luminescence behavior. TZPP shows obvious AIE character, whereas TZPE gives bright emission in both solution and solid. Based on the spectral measurement and theoretical analysis, it is found that the stereochemistry of exocyclic C=N double bond in the first excited state ($S_1$) leading to the transformation between local excited (LE) state and twisted intramolecular charge transfer (TICT) state is the crucial factor for AIE formation, which could be vividly described as restriction of conformation transformation in excited state (RCTES). Enjoying this process, a series of TZPP-based derivates are attempted, and all of them still maintain the AIE characteristics, demonstrating that TZPP based on *E*/*Z* transformation of the C=N bond is indeed a novel building block for AIEgens construction.

## RESULTS

The TZPP and TZPE are synthesized under mild conditions from commercial 2-amiopyridines (**1**) and the corresponding isothiocyanates (**2**) in 83% and 86% yields, which are not sensitive to air and water (Scheme 2A and Figures S1–S5). The two compounds are characterized using $^{1}$H NMR, $^{13}$C NMR, and mass spectra. Satisfactory data corresponding to their structures are obtained. The crystal structures from X-ray crystallography analysis are displayed in Scheme 2B-2E and Figure S6. The angles ($\phi$) of the C(6)–N(3)–C(7) in TZPP and TZPE are 121.5° and 114.7°, respectively, indicating their preferential *Z*-conformation. The molecular packing of TZPP shows an antiparallel arrangement, in which TZP and phenyl units form a head-to-tail stacking. In addition, apart from H-H repulsive force, multiple intermolecular interactions, including the weak π-π stacking interactions among TZP units, C–H···N interactions, N···N interactions, and C–H···π interactions appearing in the four adjacent benzene rings in the crystal, also play an important role in locking the rotation of benzene ring and further retaining the absolute *Z*-configuration (Viglianti et al., 2017; Mei et al., 2014; Xu et al., 2015). By contrast, the TZP units in TZPE show a face-to-face stacking with a distance of 3.403 Å, and the distances of intermolecular interactions, including C–H···N, S···S, and C–H···π are 2.631 Å, 3.876 Å, and 3.180 Å/2.896 Å, respectively. The different packing mode and intermolecular interactions in TZPP and TZPE could bring different photophysical behavior in aggregates.

As shown in Figures 1A and 1D, the UV absorption and PL spectra of TZPP and TZPE are investigated in dilute THF solution and solid states. They exhibit similar absorption bands around at 290 and 380 nm.

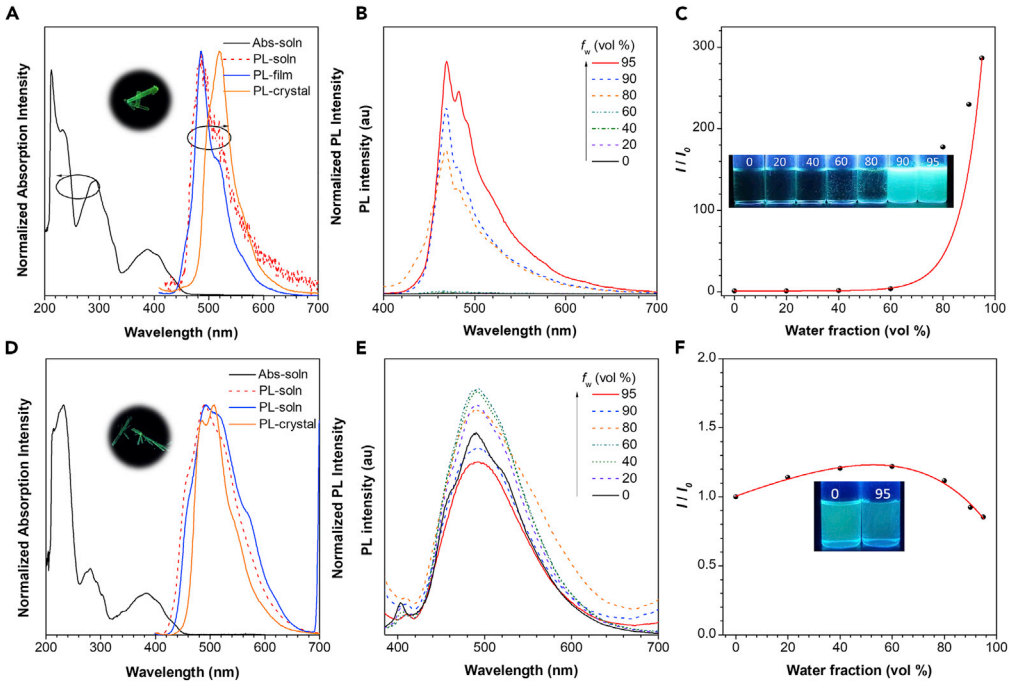


**Figure 1. Optical Characteristics of TZPP and TZPE**

(A and D) Absorption spectra of TZPP/TZPE in $10^{-5}$ M THF solution; photoluminescence (PL) spectra of TZPP in $10^{-3}$ M THF solution and solid state/TZPE in $10^{-5}$ M THF solution and solid state.

(B and E) TZPP and TZPE in THF-water mixtures with different water fractions ($f_w$).

(C and F) Plots of $I/I_o$ versus the $f_w$; $I_o$ is the PL intensity in pure THF. Concentration = $10^{-3}$ M. Inset: Photographs of the corresponding luminogens in THF-water mixtures ($f_w$ = 0–95%), taken under the illumination of a UV lamp (365 nm).

Compared with TZPE, the former absorption peak of TZPP has greater absorption intensity due to the conjugation expanding effect from phenyl substituents, implying that these absorption bands might be originated from the π-π* transition of TZP. Interestingly, the PL emission of TZPP in THF could be detected until its concentration was up to $10^{-3}$ M, locating at around 487 nm with quite weak intensity, and its fluorescence quantum yield ($\Phi_F$) was only 0.6%. In contrast, TZPE gives bright sky-blue emission at 490 nm with $\Phi_F$ of 10.0%. When they are fabricated into neat films, the emission intensity of TZPP is enhanced obviously with peaking at around 486 nm, and its $\Phi_F$ reaches 15.4% (25.7 times increment), which is indicative of its AIE nature. The $\Phi_F$ of TZPE increases to 16.8%, presenting aggregation-enhanced emission behavior to some extent (Reddy et al., 2019; Zhang et al., 2018). TZPP and TZPE could also luminesce strongly in crystal states, showing PL peaks at 519 and 508 nm with enhanced $\Phi_F$ of 16.2% and 17.9%, respectively. Their constants of the radiative rate ($k_r$) and non-radiative rate ($k_{nr}$) in different states are estimated according to the kinetic parameters from lifetime measurement (Table 1 and Figure S7). It can be seen that the $k_{nr}$ of both the compounds show decrement from solutions to solid states, corresponding to the process of restriction of intermolecular motions (RIMs) (Feng et al., 2018; Hong et al., 2009), which is conductive to the higher $\Phi_F$ in the solid state. However, different from the fast and steady $k_r$ of TZPE in various states, the $k_r$ of TZPP is quite slow in solution and exhibits a dramatic increase from solution to solid state, which probably gives rise to the "turn-on" luminescence. Therefore, besides the RIM mechanism, we supposed that a new mechanism could exist and play a significant role in the AIE behavior of TZPP.

To further validate their different AIE activities, the emission behaviors of the two compounds in the THF/water mixture are investigated (Figures 1B, 1C, 1E and 1F). The PL intensity of TZPP remains low when the water fraction ($f_w$, vol %) is less than 60%. By adding a large amount of water ($f_w \geq 60\%$) to the THF solution, the nanoaggregates of TZPP are readily formed, and the PL intensity increased accordingly. Finally, stronger PL intensity is observed with higher water fraction used ($f_w$ = 95%) (Figure S8). For TZPE, the aggregation process shows no significant effect on the intensity of the PL peaks. The slight PL drop as the $f_w$ increased may be ascribed to the aggregate size effect (Yu et al., 2018a; Jiang et al., 2017).

| Sample | $\lambda_{abs}$[a] (nm) | $\lambda_{em}$ (nm) [$\Phi_F$[d] (%)] | | | $a_{AIE}$[e] | $\tau$[f] (ns) [$k_r$ ($ns^{-1}$), $k_{nr}$ ($ns^{-1}$)] | | |
|---|---|---|---|---|---|---|---|---|
| | | THF | Film[c] | Crystal | | THF | Film | Crystal |
| TZPP | 389 | 487[b] (0.6) | 486 (15.4) | 519 (16.2) | 25.6 | 2.82 (0.002, 0.352) | 4.83 (0.032, 0.175) | 6.14 (0.026, 0.136) |
| TZPE | 382 | 490 (10.0) | 493 (16.8) | 508 (17.9) | 1.68 | 5.32 (0.019, 0.169) | 7.50 (0.022, 0.111) | 8.17 (0.022, 0.100) |

**Table 1. Optical Properties of Luminogens Based on TZPP and TZPE**

$k_r$ = radiative decay rate ($k_r = \Phi_F/\tau$); $k_{nr}$= nonradiative decay rate [$k_{nr} = (1-\Phi_F)/\tau$]

[a]In THF solution ($10^{-5}$ M).

[b]In THF solution ($10^{-3}$ M).

[c]Drop-casted film on quartz plate.

[d]Fluorescence quantum yield, determined by a calibrated integrating sphere.

[e]Values of AIE effect, calculated by $\Phi_F$ (film)/ $\Phi_F$ (soln).

[f]Fluorescence lifetime, measured at room temperature in air.

To gain a deeper insight into the photophysical behavior differences between TZPP and TZPE, theoretical investigation on these two compounds is performed in both solution and solid state by using density functional theory (DFT) and time-dependent DFT. The solvation effect and aggregation effect are considered by using the polarizable model and ONIOM method with QM and MM layers in Gaussian 16 program, respectively. The universal force field (UFF) is used with the restrained electrostatic potential partial charges for the MM treatment. The computation models (Figure S9) are built by digging a cluster from the X-ray crystal structures.

To shed light on the stereochemistry of C=N double bond and its function during the photophysical process, the optimized *Z*- and *E*-geometries of TZPP are investigated at the same time. The results of geometry optimization with frontier molecular orbitals and energy gaps performed for $S_0$ and $S_1$ in solution state are summarized in Figure 2 and Table S1. At $S_0$, the geometry of isomers changes mainly around the C=N double bond as the C6–N3 bond length decreases slightly with central dihedral angle S1–C6–N3–C7 ($\theta$) twisted from 3.6° ($S_0$-1) to 168.8° ($S_0$-2). Meanwhile, the distribution characters of electronic orbitals (HOMO→ LUMO) are almost the same, which are consistent with the calculated absorption energy results of isomers, but the data differ widely at $S_1$. These two optimized geometries at $S_1$ can be easily distinguished as LE state and TICT state according to their specific electronic distribution (Naito et al., 2017; Li et al., 2018). The former one ($S_1$-1) is mainly dominated by electronic local excitation on the whole molecular backbone, whereas the latter one ($S_1$-2) is totally a charge transfer from the TZP unit to phenyl part. The optimization geometries of these two minimums are further compared at $S_1$, which showed that the C6–N3 bond length changed from 1.271 Å at $S_0$ to 1.306 Å at LE state/1.381 Å at TICT state, together with the central dihedral $\theta$ twisted from 3.6° to 31.1°/112.1°, respectively. All these differences in geometries finally result in the practically different distribution character of the electrons (main bond length and angles are presented in Table S2). The LE state with a visible emission at 450 nm possesses a much larger oscillator strength (0.2038) than that of the TICT state (0.0011), which agrees well with the extremely weak experimental emission at 487 nm but fails to explain the low quantum yield in solution.

To solve the mystery of the almost no fluorescent behavior of TZPP in solution, the potential energy surfaces (PESs), as indicated by the optimized geometries of TZPP at $S_1$ state, were obtained along the central dihedral angle $\theta$ via scanning relaxed geometries at $S_0$ and $S_1$ states, respectively. As suggested in Figure 2, "double wells" are exhibited in both PESs at $S_0$ and $S_1$ states of TZPP in solution. For $S_0$ they correspond to the typical *Z*- and *E*-geometries, and the *Z* one is more stable, in good agreement with the single-crystal X-ray structure. Different from the large energy barrier (0.77 eV) for isomerization at $S_0$ state, the two local minima of $S_1$ have a very low barrier of 0.05 eV, which means they can undergo fast conformation conversion before deactivation process back to the ground state. Meanwhile, TICT state has an invisible emission at 869 nm (Figure S10), suggesting that it is a dark state inclined back to the ground state through a faster nonradiative transition process. It is confirmed that the weak emission in solution comes from the trace LE state (Figure S11), but most of the excited state energy "dropped" to the dark state (TICT). A conclusion could be drawn that the low energy gap between LE and TICT state in TZPP makes it easy for undergoing fast structural relaxation at $S_1$ and finally results in a low fluorescence quantum yield in solution.

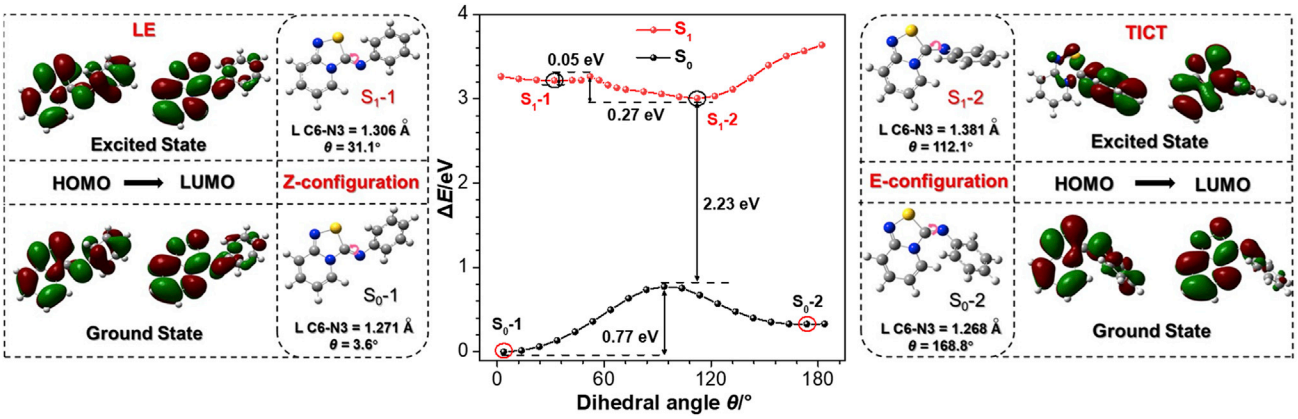


**Figure 2. Optimized Geometries of TZPP at $S_0$ and $S_1$, Frontier Molecular Orbitals of TZPP at $S_0$ and $S_1$, and PESs along the Central Dihedral Angle S1-C6-N3-C7 ($\theta$) of TZPP by Scanning Relaxed Geometries in THF**

According to our calculation results in solid state of TZPP, it is impossible to proceed with the geometry transformation between LE and TICT at $S_1$ state as it only has an LE emission at 417 nm due to the large shift barrier (Table S3, Figure S12), which further reinforces the correctness of our hypothesis that the C=N double bond structure is essential for the AIE phenomenon of TZPP. All calculations performed in solid state do not include the intermolecular vibrionic coupling, which would result in hypochromic shift of emission.

However, this advantage of structure becomes functionless when combined with ethyl group because no similar electronic distribution trend of TZPE could be found at the $S_1$ state with the central dihedral angle $\theta$ gradually twisted in solution, and the distribution of electrons almost has no change at the same time, indicating that the de-excitation process of $S_1$ always concentrates on the TZP moiety (Figure S13). Not surprisingly, the calculated results at $S_1$ in solid state of TZPE show the same LE characteristics with the same emission at 422 nm (Table S4), which agrees well with the experimental fluorescence data. Comparing the geometries and transition orbitals of TZPP and TZPE, we find that the electronic effects of the substituent on C=N double bond could make big differences in the electronic distribution for photophysical behavior. It should be the stereochemistry of the C=N double bond and the electronic properties of the substituents attached to the N atom that co-determine the nature of the AIE phenomenon of TZPP, suppressing the conformation conversion between LE and TICT states from solution to solid state.

To explore the universality of this new AIEgen (TZPP), we try to decorate it at the C-3/C-4 position of the pyridine ring or C-10 position of the phenyl ring with commonly used electron-donating groups (triphenylamine and carbazole). The halo-substituted products can readily undergo Suzuki-Miyaura coupling reaction to afford the corresponding arylated products (Figure 3 and S14–S15). After a simple separation operation using silica gel column chromatography, the purified products are obtained in good yields. The structures of Cz-3-TZPP, TPA-4-TZPP, and TPA-10-TZPP are also clarified by single-crystal X-ray analysis. Excitingly, all TZPP-based derivatives have the stable *Z*-configuration in solid state. Then, a series of photophysical properties are also studied (Table 2, Figure 4, and S16–18). The TZPP-based derivatives show semblable AIE properties, in which weak fluorescence intensity ($\Phi_F$ < 1%) is detected in THF solutions, whereas intensive emission is observed by forming aggregates. From solutions to neat films, all derivatives show an order of magnitude increase in the constants of $k_r$, corresponding to the process of RCTES, which gives rise to the "turn-on" luminescence. In addition, these derivates are not sensitive to external stimuli, such as temperature, organic solvent vapors, and mechanical force (Figure S19). It should be noted that the enlarged conjugate system allows the molecule to emit more efficiently ($\Phi_F$ = 28.1%) in modifying the pyridine ring at the C-3 position, which provides a new guiding direction for further molecular modification. Meanwhile, the packing mode of the substitutes in TZPP-based derivatives could also have an impact on the variation of $k_{nr}$, leading to their different $\Phi_F$. These PL spectra accord with the theoretical calculation that they exhibit LE and TICT transformation (Figure S20 and Table S5). Thus, the TZPP compound should not only be an AIEgen but also be a typical AIE building block.

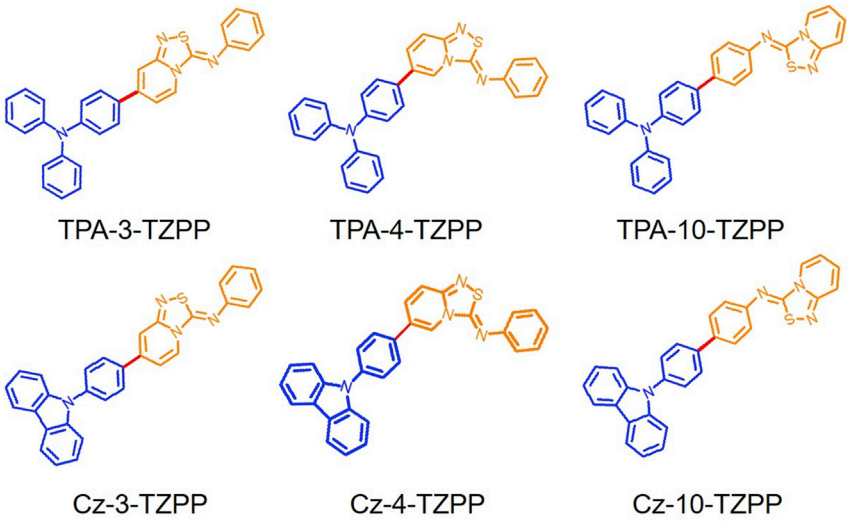


**Figure 3. Structures of TZPP-Based Derivates**

## DISCUSSION

In summary, a novel design of AIE building block based on EZI has been developed. Through stable exocyclic C=N double bond, the pristine TZPP is reported as an AIE core, which could be synthesized under mild conditions with commercial 2-amiopyridine and isothiocyanate. Theoretical calculations show that the crucial factor of AIE behaviors in TZPP is the stereochemistry change of intramolecular C=N double bond and the corresponding transformation between LE and TICT states from solution to solid state, which is consistent with a series of spectral experiments. In addition, these TZPP-based derivatives exhibit similar AIE behaviors, which affords a clear and specific strategy for constructing and decorating AIEgens in further work. It is believed that the compound TZPP and TZPP-based derivatives will not only be explored as the virgin territory of AIEgens but also be beneficial to provide design guidelines for the development of new AIE systems and practical applications.

### Limitations of the Study

In this work, the fluorescence quantum yields of AIEgens based on TZPP core are relatively low in solid state. Subsequent work should be carried out on improving the fluorescence efficiency.

| Sample | $\lambda_{abs}$[a] (nm) | $\lambda_{em}$ (nm) | | $\Phi_F$[d] (%) | | $a_{AIE}$[e] | $\tau$[f] (ns) [$k_r$ ($ns^{-1}$), $k_{nr}$ ($ns^{-1}$)] | |
|---|---|---|---|---|---|---|---|---|
| | | THF[b] | Film[c] | THF[b] | Film[c] | | THF | Film |
| TPA-3-TZPP | 375 | 517 | 532 | 0.7 | 10.0 | 14.3 | 1.08 (0.006, 0.919) | 3.84 (0.026. 0.234) |
| Cz-3-TZPP | 340 | 524 | 539 | 0.6 | 28.1 | 46.8 | 2.95 (0.002, 0.337) | 4.74 (0.050, 0.152) |
| TPA-4-TZPP | 342 | 504 | 517 | 0.5 | 3.4 | 6.8 | 4.07 (0.001, 0.244) | 1.40 (0.024, 0.690) |
| Cz-4-TZPP | 327 | 497 | 514 | 0.8 | 4.4 | 5.5 | 3.64 (0.002, 0.272) | 1.69 (0.026, 0.565) |
| TPA-10-TZPP | 398 | 509 | 521 | 0.2 | 2.4 | 12 | 2.49 (0.001, 0.400) | 0.52 (0.046, 1.877) |
| Cz-10-TZPP | 391 | 497 | 513 | 0.2 | 2.6 | 13 | 0.57 (0.004, 1.751) | 0.54 (0.048, 1.804) |

**Table 2. Optical Properties of Luminogens Based on TZPP-Based Derivates**

$k_r$ = radiative decay rate ($k_r = \Phi_F/\tau$); $k_{nr}$= nonradiative decay rate [$k_{nr} = (1 - \Phi_F)/\tau$]

[a]In THF solution ($10^{-5}$ M).

[b]In THF solution ($10^{-3}$ M).

[c]Drop-casted film on quartz plate.

[d]Fluorescence quantum yield, determined by a calibrated integrating sphere.

[e]Values of AIE effect, calculated by $\Phi_F$ (film)/ $\Phi_F$ (soln).

[f]Fluorescence lifetime, measured at room temperature in air.

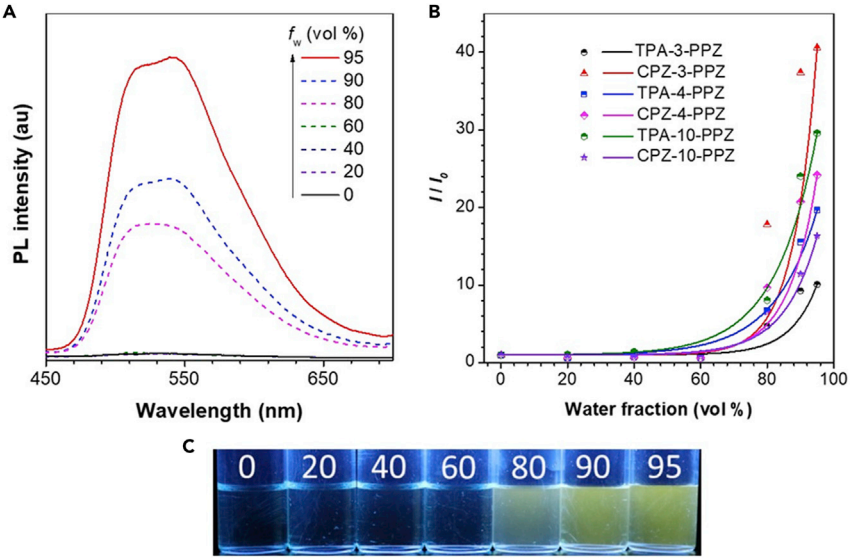


**Figure 4. Optical Characteristics of TZPP-Based Derivates**

(A) PL spectra of Cz-3-TZPP in THF/water mixtures with different water fractions ($f_w$).

(B) The plots of emission maximum and the relative emission intensity ($I/I_0$) versus the composition of the aqueous mixture of TZPP-based derivates; concentration = $10^{-5}$ M. $I_0$ = PL intensity in pure THF.

(C) Photographs of the corresponding luminogens (Cz-3-TZPP) in THF-water mixtures ($f_w$ = 0–95%), taken under the illumination of a UV lamp (365 nm).

## Resource Availability

### *Lead Contact*

Further information and requests for resources should be directed to the Lead Contact, Zhiming Wang (wangzhiming@scut.edu.cn).

### *Materials Availability*

This study did not generate new unique reagents.

### *Data and Code Availability*

The crystallography data have been deposited at the Cambridge Crystallographic Data Center (CCDC) under accession numbers CCDC: 1921846 (TZPP), CCDC: 1588922 (TZPE), CCDC: 1921837 (TPA-4-TZPP), and CCDC: 1921840 (C2-3-TZPP) and can be obtained free of charge from www.ccdc.cam.ac.uk/getstructures.

## METHODS

All methods can be found in the accompanying Transparent Methods supplemental file.

## SUPPLEMENTAL INFORMATION

Supplemental Information can be found online at https://doi.org/10.1016/j.isci.2020.101587.

## ACKNOWLEDGMENTS

This work is financially supported by the National Key Research and Development Program of China (2016YFA0602900), National Natural Science Foundation of China (21472051, 21788102, 51673118, 21975077), the Innovation and Technology Commission of Hong Kong (ITC-CNERC14SC01), Science & Technology Program of Guangzhou (201804020027, 201804010218), and the Fundamental Research Funds for the Central Universities (2019ZD04).

CellPress
OPEN ACCESS

## AUTHOR CONTRIBUTIONS

W.Y. discovered the reaction, synthesized the reagents and substrates, and performed the experimental studies; H.Z. assisted the experimental studies, analyzed the data, and contributed to the redaction of the manuscript; P.-A.Y. performed the theoretical calculation and contributed to the writing of the theoretical calculation; F.Z. assisted the experimental studies; Z.W. devised and supervised the experiments and contributed to the redaction of the manuscript; Q.P. gave the guidance of theoretical calculation; W.W. gave the guidance of synthesis and contributed to the redaction of the manuscript; H.J. and B.Z.T managed the overall project, designed the reactions, planned the experiments, and participated in the redaction of the manuscript.

## DECLARATION OF INTERESTS

The authors declare no competing interests.

Received: June 12, 2020
Revised: August 10, 2020
Accepted: September 14, 2020
Published: October 23, 2020

## REFERENCES

Belowicha, M.E., and Stoddart, J.F. (2012). Dynamic imine chemistry. Chem. Soc. Rev. *41*, 2003–2024.

Berenbeim, J.A., Boldissar, S., Owens, S., Haggmark, M.R., Gate, G., Siouri, F.M., Cohen, T., Rode, M.F., Schmidt Patterson, C., and DeVries, M.S. (2019). Excited state intramolecular proton transfer in hydroxyanthraquinones: toward predicting fading of organic red colorants in art. Sci. Adv. *5*, eaaw5227.

Cai, Y., Du, L., Samedov, K., Gu, X., Qi, F., Sung, H.H.Y., Patrick, B.O., Yan, Z., Jiang, X., Zhang, H., et al. (2018). Deciphering the working mechanism of aggregation-induced emission of tetraphenylethylene derivatives by ultrafast spectroscopy. Chem. Sci. *9*, 4662–4670.

Chen, Y., Lam, J.W.Y., Kwok, R.T.K., Liu, B., and Tang, B.Z. (2019). Aggregation-induced emission: fundamental understanding and future developments. Mater. Horiz. *6*, 428–433.

Feng, G., and Liu, B. (2018). Aggregation-induced emission (AIE) dots: emerging theranostic nanolights. Acc. Chem. Res. *51*, 1404–1414.

Feng, H., Yuan, Y., Xiong, J., Zheng, Y., and Tang, B.Z. (2018). Macrocycles and cages based on tetraphenylethylene with aggregation-induced emission effect. Chem. Soc. Rev. *47*, 7452–7476.

Gon, M., Tanaka, K., and Chujo, Y. (2018). A highly efficient near-infrared-emissive copolymer with a N=N double-bond Π-conjugated system based on a fused azobenzene-boron complex. Angew. Chem. Int. Ed. *57*, 6546–6551.

He, D., Zhuang, Z., Wang, X., Li, J., Li, J., Wu, W., Zhao, Z., Jiang, H., and Tang, B.Z. (2019). Assembly of 1H-isoindole derivatives by selective carbon–nitrogen triple bond activation: access to aggregation-induced emission fluorophores for lipid droplet imaging. Chem. Sci. *10*, 7076–7081.

Hong, Y., Lam, J.W., and Tang, B.Z. (2009). Aggregation-induced emission: phenomenon, mechanism and applications. Chem. Commun. *29*, 4332–4353.

Hu, F., Xu, S., and Liu, B. (2018). Photosensitizers with aggregation-induced emission: materials and biomedical applications. Adv. Mater. *30*, 1801350.

Jiang, M., Gu, X., Lam, J.W.Y., Zhang, Y., Kwok, R.T.K., Wong, K.S., and Tang, B.Z. (2017). Two-photon AIE bio-probe with large Stokes shift for specific imaging of lipid droplets. Chem. Sci. *8*, 5440–5446.

Kokado, K., and Sada, K. (2019). Consideration of molecular structure in the excited state to design new luminogens with aggregation-induced emission. Angew. Chem. Int. Ed. *58*, 8632–8639.

Kokado, K., Machida, T., Iwasa, T., Taketsugu, T., and Sada, K. (2018). Twist of C=C bond plays a crucial role in the quenching of AIE-active tetraphenylethene derivatives in solution. J. Phys. Chem. C *122*, 245–251.

Kwok, R.T.K., Leung, C.W., Lam, J.W.Y., and Tang, B.Z. (2015). Biosensing by luminogens with aggregation-induced emission characteristics. Chem. Soc. Rev. *44*, 4228–4238.

Li, J., Yang, C., Peng, X., Chen, Y., Qi, Q., Luo, X., Lai, W., and Huang, W. (2018). Stimuli-responsive solid-state emission from *o*-carborane-tetraphenylethene dyads induced by twisted intramolecular charge transfer in the crystalline state. J. Mater. Chem. C *6*, 19–28.

Lu, H., Wang, K., Liu, B.B., Wang, M., Huang, M.M., Zhang, Y., and Yang, J.P. (2019). Systematic oligoaniline-based derivatives: ACQ-AIE conversion with a tunable insertion effect and quantitative fluorescence "turn-on" detection of BSA. Mater. Chem. Front. *3*, 331–338.

Luo, J., Xie, Z., Lam, J.W.Y., Cheng, L., Chen, H., Qiu, C., Kwok, H.S., Zhan, X., Liu, Y., Zhu, D., and Tang, B.Z. (2001). Aggregation-induced emission of 1-methyl-1,2,3,4,5-pentaphenylsilole. Chem. Commun. *18*, 1740–1741.

Mei, J., Hong, Y., Lam, J.W.Y., Qin, A., Tang, Y., and Tang, B.Z. (2014). Aggregation-induced emission: the whole is more brilliant than the parts. Adv. Mater. *26*, 5429–5479.

Mei, J., Leung, N.L.C., Kwok, R.T.K., Lam, J.W.Y., and Tang, B.Z. (2015). Aggregation-induced emission: together we shine, united we soar! Chem. Rev. *115*, 11718–11940.

Naito, H., Nishino, K., Morisaki, Y., Tanaka, K., and Chujo, Y. (2017). Solid-state emission of the anthracene-*o*-carborane dyad from the twisted-intramolecular charge transfer in the crystalline state. Angew. Chem. Int. Ed. *56*, 254–259.

Padalkar, V.S., and Seki, S. (2016). Excited-state intramolecular proton-transfer (ESIPT)-Inspired solid state emitters. Chem. Soc. Rev. *45*, 169–202.

Qian, J., and Tang, B.Z. (2017). AIE luminogens for bioimaging and theranostics: from organelles to animals. Chem *3*, 56–91.

Reddy, T.S., Shin, S.H., and Choi, M.S. (2019). Effects of molecular flexibility/rigidity on the AIE/AIEE properties of aromatic thiols-substituted 1,8-naphthalimides. Dyes Pigm. *160*, 483–491.

Sasaki, S., Suzuki, S., Sameera, W.M.C., Igawa, K., Morokuma, K., and Konishi, G.-i. (2016). Highly twisted *N*,*N*-dialkylamines as a design strategy to tune simple aromatic hydrocarbons as steric environment-sensitive fluorophores. J. Am. Chem. Soc. *138*, 8194–8206.

Sedgwick, A.C., Wu, L., Han, H.-H., Bull, S.D., He, X.-P., James, T.D., Sessler, J.L., Tang, B.Z., Tian, H., and Yoon, J. (2018). Excited-state intramolecular proton-transfer (ESIPT) based fluorescence sensors and imaging agents. Chem. Soc. Rev. *47*, 8842–8880.

Shustova, N.B., Ong, T.C., Cozzolino, A.F., Michaelis, V.K., Griffin, R.G., and Dinca, M. (2012). Phenyl ring dynamics in a tetraphenylethylene-bridged metal-organic framework: implications for the mechanism of aggregation-induced emission. J. Am. Chem. Soc. *134*, 15061–15070.

Sturala, J., Etherington, M.K., Bismillah, A.N., Higginbotham, H.F., Trewby, W., Aguilar, J.A.,

Bromley, E.H.C., Avestro, A.-J., Monkman, A.P., and McGonigal, P.R. (2017). Excited-state aromatic interactions in the aggregation-induced emission of molecular rotors. J. Am. Chem. Soc. *139*, 17882–17889.

Suzuki, N., Fukazawa, A., Nagura, K., Saito, S., Kitoh-Nishioka, H., Yokogawa, D., Irle, S., and Yamaguchi, S. (2014). A strap strategy for construction of an excited-state intramolecular proton transfer (ESIPT) system with dual fluorescence. Angew. Chem. Int. Ed. *53*, 8231–8235.

Tang, X., Wu, W., Zeng, W., and Jiang, H. (2018). Copper-catalyzed oxidative carbon-carbon and/or carbon-heteroatom bond formation with $O_2$ or internal oxidants. Acc. Chem. Res. *51*, 1092–1105.

Tong, S., Zhao, S., He, Q., Wang, Q., Wang, M.-X., and Zhu, J. (2017). Fluorophores for excited-state intramolecular proton transfer by an yttrium triflate catalyzed reaction of isocyanides with thiocarboxylic acids. Angew. Chem. Int. Ed. *56*, 6599–6603.

Tseng, N.-W., Liu, J., Ng, J.C.Y., Lam, J.W.Y., Sung, H.H.Y., Williams, I.D., and Tang, B.Z. (2012). Deciphering mechanism of aggregation-induced emission (AIE): is E-Z isomerisation involved in an AIE process? Chem. Sci. *3*, 493–497.

Tseng, H.-W., Shen, J.-Y., Kuo, T.-Y., Tu, T.-S., Chen, Y.-A., Demchenko, A.P., and Chou, P.-T. (2016). Excited-state intramolecular proton-transfer reaction demonstrating anti-kasha behavior. Chem. Sci. *7*, 655–665.

Tu, Y., Liu, J., Zhang, H., Peng, Q., Lam, J.W.Y., and Tang, B.Z. (2019). Restriction of access to the dark state: a new mechanistic model for heteroatom-containing AIE systems. Angew. Chem. Int. Ed. *58*, 14911–14914.

Viglianti, L., Leung, N.L.C., Xie, N., Gu, X., Sung, H.H.Y., Miao, Q., Williams, I.D., Licandro, and Tang, B.Z. (2017). Aggregation-induced emission: mechanistic study of the clusteroluminescence of tetrathienylethene. Chem. Sci. *8*, 2629–2639.

Wang, X., He, D., Huang, Y., Fan, Q., Wu, W., and Jiang, H. (2018). Copper-catalyzed synthesis of substituted quinazolines from benzonitriles and 2-ethynylanilines via carbon–carbon bond cleavage using molecular oxygen. J. Org. Chem. *83*, 5458–5466.

Wang, B.-W., Jiang, K., Li, J.-X., Luo, S.-H., Wang, Z.-Y., and Jiang, H.-F. (2019a). 1,1-Diphenylvinylsulfide as a functional AIEgen derived from the aggregation-caused-quenching molecule 1,1-diphenylethene through simple thioetherification. Angew. Chem. Int. Ed. *59*, 2338–2343.

Wang, W., Marshall, M., Collins, E., Marquez, S., Mu, C., Bowen, K.H., and Zhang, X. (2019b). Intramolecular electron-induced proton transfer and its correlation with excited-state intramolecular proton transfer. Nat. Commun. *10*, 1170.

Wei, Q., Fei, N., Islam, A., Lei, T., Hong, L., Peng, R., Fan, X., Chen, L., Gao, P., and Ge, Z. (2018a). Small-molecule emitters with high quantum efficiency: mechanisms, structures, and applications in OLED devices. Adv. Opt. Mater. *6*, 1800512.

Wei, P., Zhang, J., Zhao, Z., Chen, Y., He, X., Chen, M., Gong, J., Sung, H.H.Y., Williams, I.D., Lam, J.W.Y., and Tang, B.Z. (2018b). Multiple yet controllable photoswitching in a single AIEgen system. J. Am. Chem. Soc. *140*, 1966–1975.

Xie, Y., and Li, Z. (2019). Recent advances in Z/E-Isomers of tetraphenylethene derivatives: AIE mechanism, photophysical property, chemical probe, and stereoselectivity syntheses. Chem-Asian J. *14*, 2524–2541.

Xiong, J.-B., Yuan, Y.-X., Wang, L., Sun, J.-P., Qiao, W.-G., Zhang, H.-C., Duan, M., Han, H., Zhang, S., and Zheng, Y.-S. (2018). Evidence for aggregation-induced emission from free rotation restriction of double bond at excited state. Org. Lett. *20*, 373–376.

Xu, B., He, J., Mu, Y., Zhu, Q., Wu, S., Wang, Y., Zhang, Y., Jin, C., Lo, C., Chi, Z., et al. (2015). Very bright mechanoluminescence and remarkable mechanochromism using a tetraphenylethene derivative with aggregation-induced emission. Chem. Sci. *6*, 3236–3241.

Yu, Y., Xu, Z., Zhao, Z., Zhang, H., Ma, D., Lam, J.W.Y., Qin, A., and Tang, B.Z. (2018a). In situ generation of red-emissive AIEgens from commercial sources for nondoped OLEDs. ACS Omega *3*, 16347–16356.

Yu, W., Huang, Y., Li, J., Tang, X., Wu, W., and Jiang, H. (2018b). Copper-catalyzed aerobic oxidative [3+2] annulation for the synthesis of 5-amino/imino-substituted 1,2,4-thiadiazoles through C-N/N-S bond formation. J. Org. Chem. *83*, 9334–9343.

Zhang, G.-F., Chen, Z.-Q., Aldred, M.P., Hu, Z., Chen, T., Huang, Z., Meng, X., and Zhu, M.-Q. (2014). Direct validation of the restriction of intramolecular rotation hypothesis via the synthesis of novel ortho-methyl substituted tetraphenylethenes and their application in cell imaging. Chem. Commun. *50*, 12058–12060.

Zhang, W., Yan, Y., Gu, J., Yao, J., and Zhao, Y.S. (2015). Low-threshold wavelength-switchable organic nanowire lasers based on excited-state intramolecular proton transfer. Angew. Chem. Int. Ed. *54*, 7125–7129.

Zhang, H., Zheng, X., Xie, N., He, Z., Liu, J., Leung, N.L.C., Niu, Y., Huang, X., Wong, K.S., Kwok, R.T.K., et al. (2017). Why do simple molecules with "isolated" phenyl rings emit visible light? J. Am. Chem. Soc. *139*, 16264–16272.

Zhang, W., Wang, N., Yu, Y., Shan, Y., Wang, B., Pu, X., and Yu, X. (2018). Synthetic regulation of 1,4-dihydropyridines for the AIE or AIEE effect: from rational design to mechanistic views. Chem. Eur. J. *24*, 4871–4878.

Zhang, D., Fan, Y., Chen, H., Trepout, S., and Li, M.-H. (2019). $CO_2$-Activated reversible transition between polymersomes and micelles with AIE fluorescence. Angew. Chem. Int. Ed. *58*, 10260–10265.

Zhou, P., and Han, K. (2018). Unraveling the detailed mechanism of excited-state proton transfer. Acc. Chem. Res. *51*, 1681–1690.

Zhou, P., Li, P., Zhao, Y., and Han, K. (2019). Restriction of flip-flop motion as a mechanism for aggregation-induced emission. J. Phys. Chem. Lett. *10*, 6929–6935.

iScience, Volume *23*

## Supplemental Information

# Restriction of Conformation Transformation in Excited State: An Aggregation-Induced Emission Building Block Based on Stable Exocyclic C=N Group

**Wentao Yu, Han Zhang, Ping-An Yin, Fan Zhou, Zhiming Wang, Wanqing Wu, Qian Peng, Huanfeng Jiang, and Ben Zhong Tang**

**Transparent Methods.**

**General information.**

All reagents were purchased from commercial sources and used as received without further purification. NMR spectra were recorded in $CDCl_3$, on a 400 MHz spectrometer. Chemical shifts were reported in parts per million (*δ*) relative to TMS (0.00 ppm) for $^1$H NMR data and $CDCl_3$ (77.00 ppm) for $^{13}$C NMR data. IR spectra were obtained either as potassium bromide pellets or as liquid films between two potassium bromide pellets with an infrared Fourier spectrometer. High-resolution mass spectra (ESI) were obtained with a LCMS-IT-TOF mass spectrometer. UV-vis absorption spectra were measured on a Shimadzu UV-2600 spectrophotometer. Photoluminescence spectra were recorded on a Horiba Fluoromax-4 spectrofluorometer. Solution fluorescence quantum yields were measured using a Hamamatsu absolute PL quantum yield spectrometer C11347 Quantaurus_QY. Fluorescence lifetimes were determined with a Hamamatsu C11367-11 Quantaurus-Tau time-resolved spectrometer. The molecular geometry optimizations and vibrational frequencies were performed for the ground state ($S_0$) at the level of M062X/6-31G(d) and for the first singlet excited state ($S_1$) at the TDDFT/M062X/6-31G(d) level in both solution and solid states.

**Synthetic procedures and characterization for *N*-fused 1,2,4-thiadiazoles (TZPP and TZPE).**

2-Aminopyridine **1** (0.3 mmol), isothiocyanate **2** (0.45 mmol), CuI (20 mol %) and 2,4-dimethylpyridine (0.6 mmol) were mixed in 1.5 mL DCE to stir under $O_2$ balloon at 50 $^oC$. Upon completion, the reaction mixture was washed by saturated NaCl aqueous solution (2 × 10 mL) and then extracted with ethyl acetate (2 × 10 mL), and the organic layers were combined, dried over anhydrous $MgSO_4$, filtered, and concentrated under reduced pressure. The residue was separated by column chromatography (petroleum ether/ethyl acetate 20: 1) to give the pure products **3**.

**(*Z*)-*N*-(7-Methyl-3*H*-[1,2,4]thiadiazolo[4,3-*a*]pyridin-3-ylidene)-aniline (TZPP):** $^1$H NMR (400 MHz, $CDCl_3$) *δ* 8.11 (d, *J* = 7.3 Hz, 1H), 7.38 (m, 2H), 7.12 (m, 3H), 6.80 (s, 1H), 6.29 (d, *J* = 7.3 Hz, 1H), 2.25 (s, 3H).; $^{13}$C NMR (101 MHz, $CDCl_3$) *δ* 159.2, 151.7, 148.5, 144.7, 129.4, 124.8, 124.0, 121.0, 116.7, 112.3 ppm. MS (EI, 70 eV): m/z (%) = 227 $[M]^+$, 169, 124, 78, 51.

**(*Z*)-*N*-(3*H*-[1,2,4]Thiadiazolo[4,3-*a*]pyridin-3-ylidene)ethyl-1-amine (TZPE):** $^1$H NMR (400 MHz, $CDCl_3$) *δ* 7.94 (d, *J* = 7.2 Hz, 1H), 7.12 (m, 1H), 6.94 (d, *J* = 9.5 Hz, 1H), 6.38 - 6.27 (m, 1H), 3.19 (q, *J* = 7.2 Hz, 2H), 1.33 (t, *J* = 7.2 Hz, 3H); $^{13}$C NMR (100 MHz, $CDCl_3$) *δ* 158.7, 152.3, 133.3, 125.9, 119.3, 108.8, 49.2, 15.4 ppm. MS (EI, 70 eV): m/z (%) = 179 $[M]^+$, 164, 124, 78, 51.

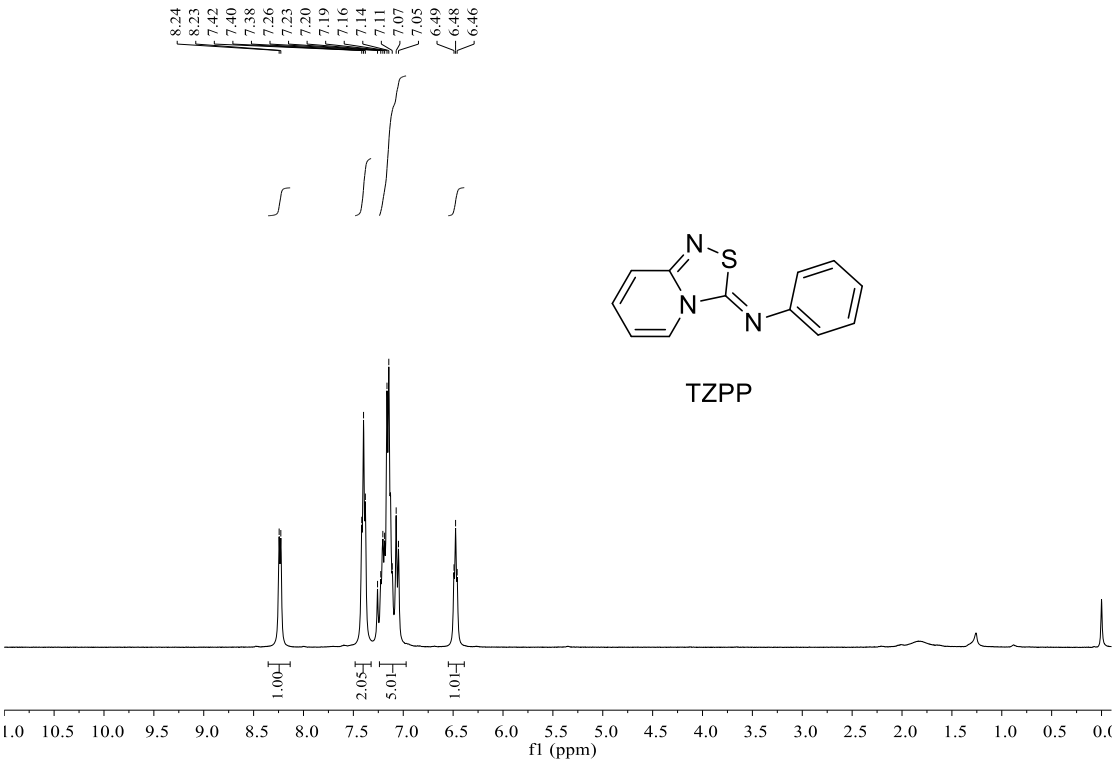


**Figure S1.** $^{1}$H NMR of TZPP in $CDCl_3$. Related to Scheme 2.

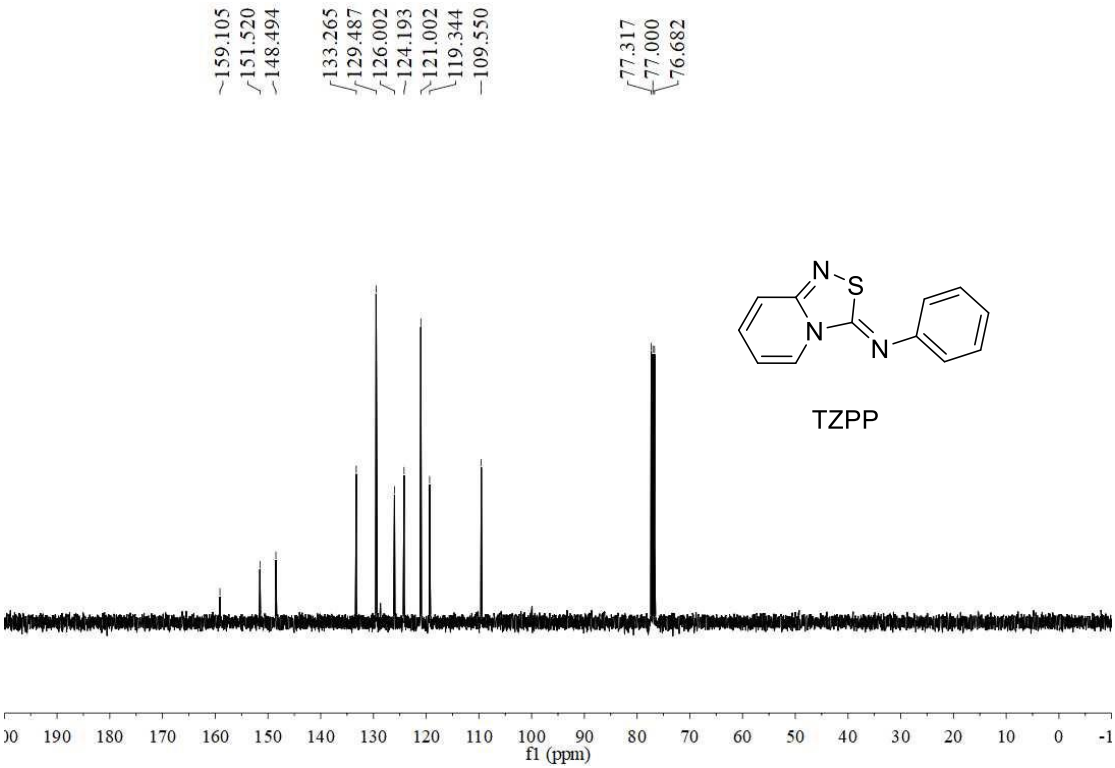


**Figure S2.** $^{13}$C NMR of TZPP in $CDCl_3$. Related to Scheme 2.

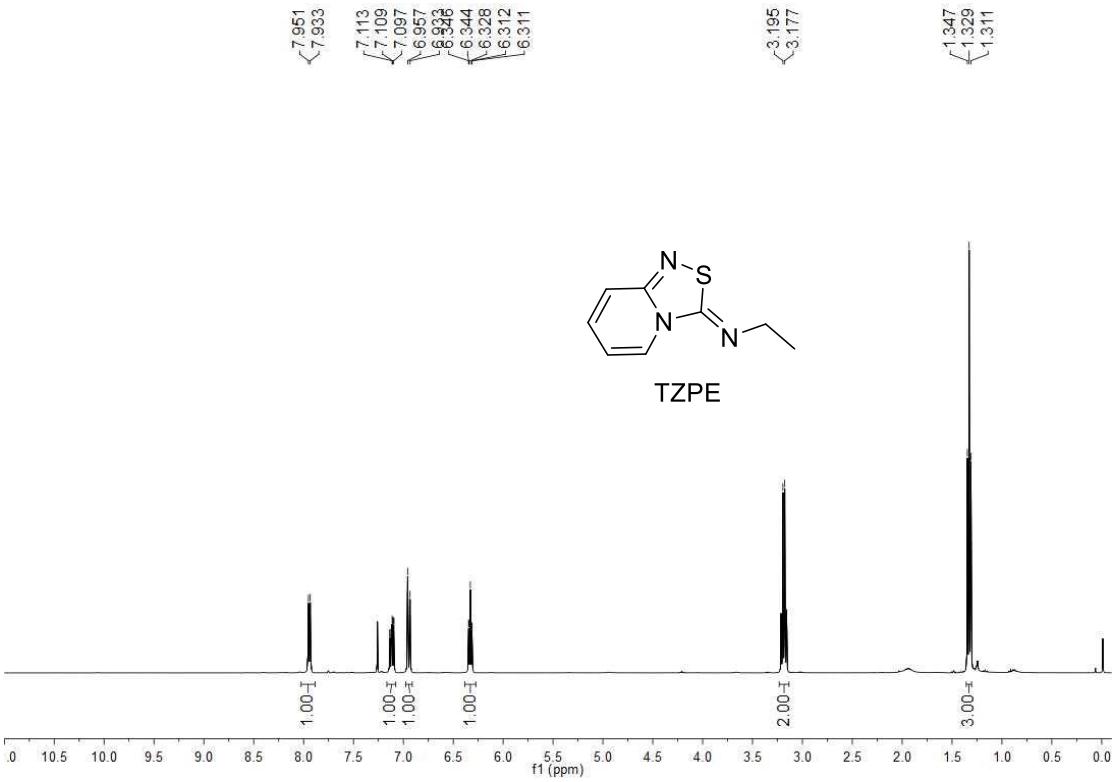


**Figure S3.** $^{1}$H NMR of TZPE in $CDCl_3$. Related to Scheme 2.

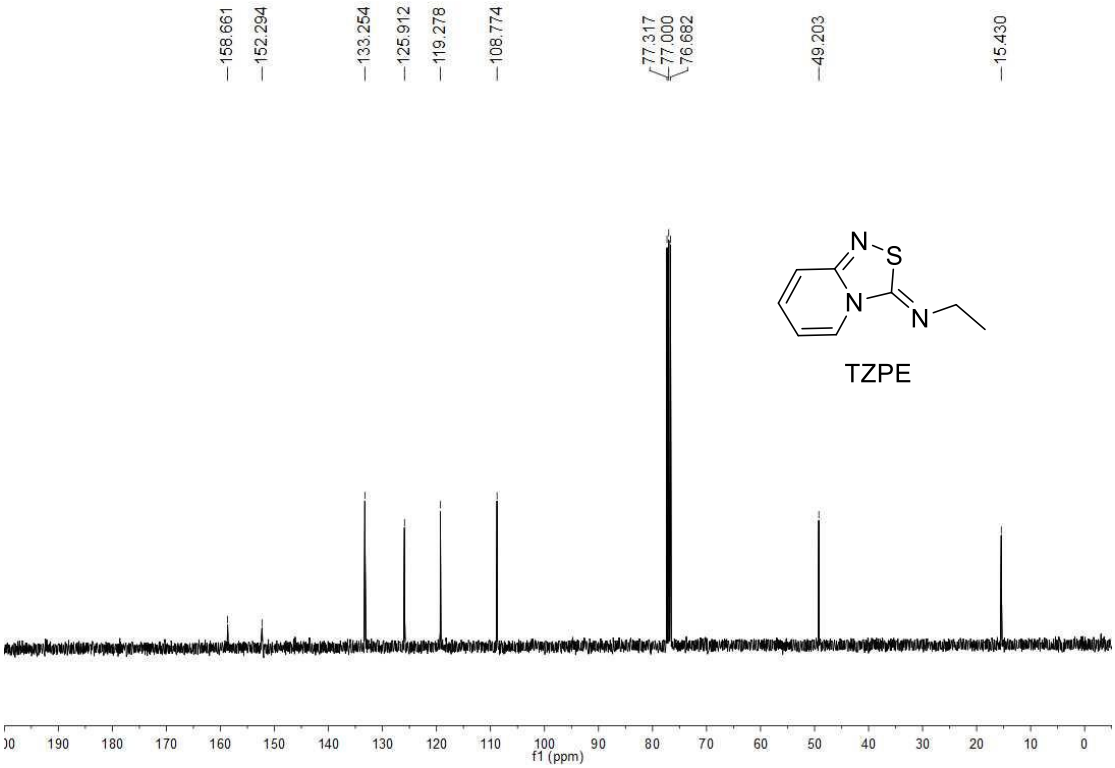


**Figure S4.** $^{13}$C NMR of TZPE in $CDCl_3$. Related to Scheme 2.

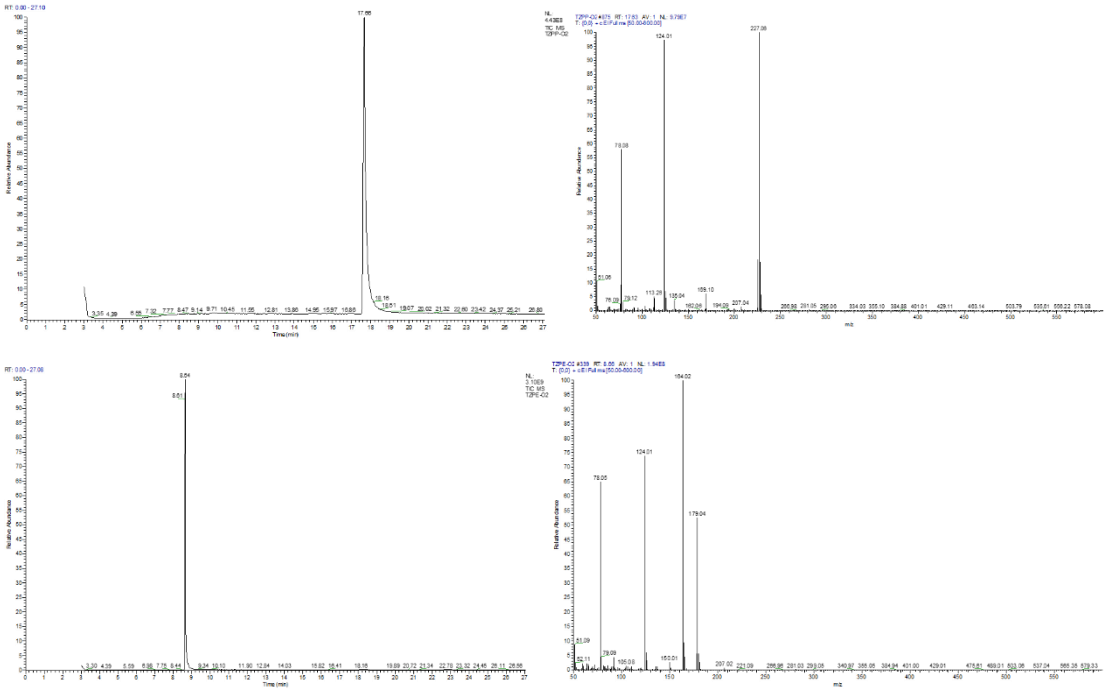

**Figure S5.** The synthesized azomethines (TZPP and TZPE) were added in water under $O_2$ atmosphere. After 7 days, they were extracted with $CH_2Cl_2$ and then were analyzed with GC-MS. Obvious artifactual bands were not observed. GC-MS of TZPP and TZPE. Related to Scheme 2.

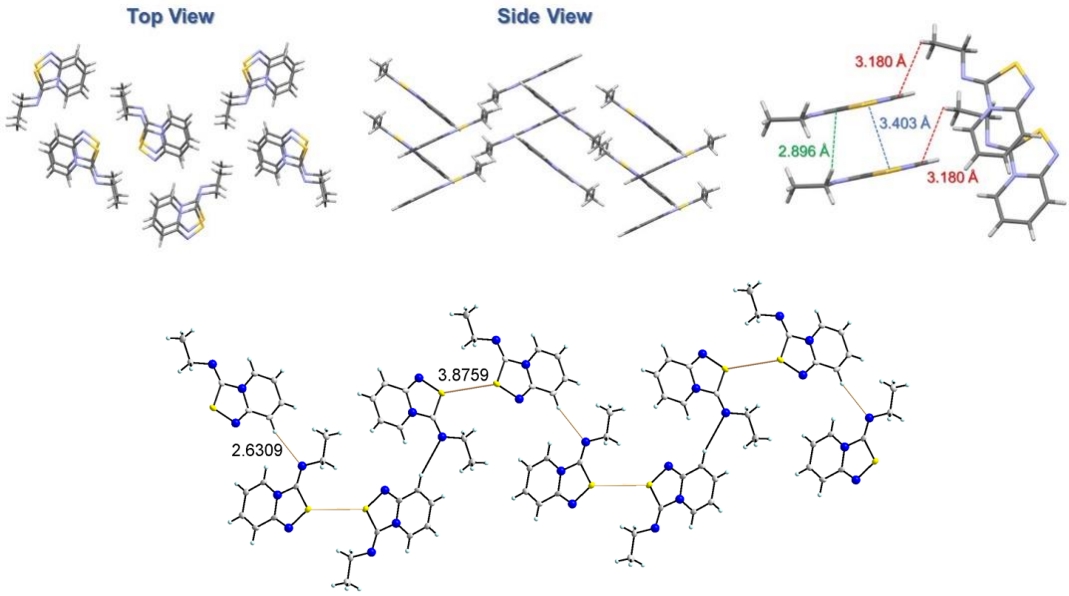


**Figure S6.** Single crystal X-ray structure analysis of TZPE. Related to Scheme 2.

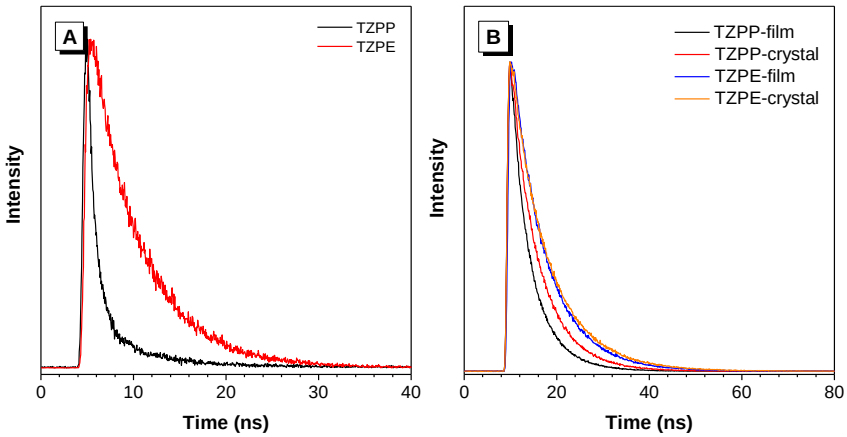


**Figure S7.** Time-resolved fluorescence decay curves of (A) in THF solutions ($10^{-5}$ M) and (B) in aggregates. Related to Table 1.

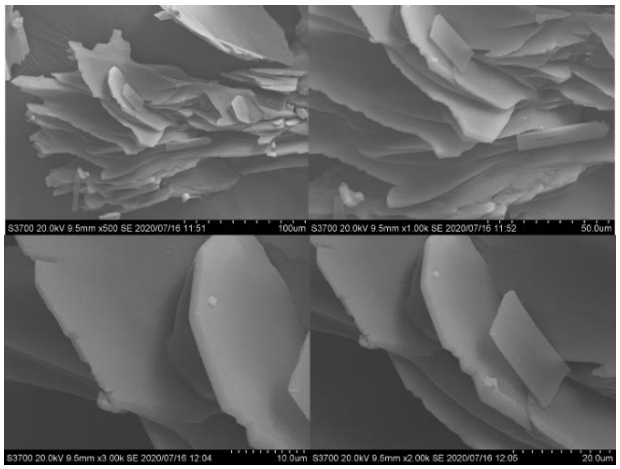

**Figure S8.** Morphology of thin films of TZPP in THF-water mixtures ($f_w$ = 95%). Related to Figure 1.

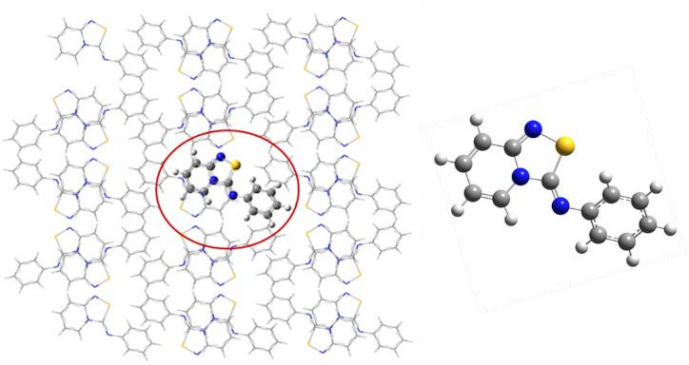

**Figure S9.** Supercell for ONIOM calculation of TZPP. Related to Figure 2.

**Table S1.** Calculated results of absorption and emission properties of TZPP in solution. Related to Figure 2.

| TZPP | | E (eV)/λ (nm) | *f* | P (HOMO->LUMO) |
|---|---|---|---|---|
| THF | $S_0$-1 | 3.67/338 | 0.1833 | 0.96 |
| | $S_0$-2 | 3.77/329 | 0.1951 | 0.98 |
| | $S_1$-1 | 2.75/450 | 0.2038 | 0.95 |
| | $S_1$-2 | 1.43/869 | 0.0011 | 0.86 |

Calculation model of solvent used in PCM method is THF.

**Table S2.** Main bond length and angles of TZPP at four states in solution. Related to Figure 2.

| TZPP | | L N1–C1 | L C1–N2 | L N2–S1 | L S1–C6 | L C6–N3 | L N3–C7 |
|---|---|---|---|---|---|---|---|
| THF | $S_0$-1 | 1.395 | 1.299 | 1.698 | 1.772 | 1.271 | 1.406 |
| | $S_0$-2 | 1.406 | 1.297 | 1.691 | 1.764 | 1.268 | 1.405 |
| | $S_1$-1 | 1.407 | 1.333 | 1.662 | 1.796 | 1.306 | 1.37 |
| | $S_1$-2 | 1.4 | 1.303 | 1.706 | 1.769 | 1.381 | 1.355 |

| TZPP | | ∠ C6–N1–C1 | ∠ N1–C1–N2 | ∠ C1–N2–S1 | ∠ N2–S1–C6 | ∠ S1–C6–N3 | ∠ C6–N3–C7 |
|---|---|---|---|---|---|---|---|
| THF | $S_0$-1 | 113.4 | 117.4 | 109.4 | 94.7 | 113.2 | 121 |
| | $S_0$-2 | 112.3 | 117.8 | 109.2 | 95.3 | 122.2 | 126.1 |
| | $S_1$-1 | 113.3 | 114.4 | 112.1 | 92.7 | 129.2 | 121 |
| | $S_1$-2 | 112.7 | 117.4 | 109.5 | 94.2 | 121.8 | 118 |

| TZPP | | *α* C6–N1–N2–S1 | *α* S1–C6–N3–C7 |
|---|---|---|---|
| THF | $S_0$-1 | -1.8 | 3.6 |
| | $S_0$-2 | 0.9 | 168.8 |
| | $S_1$-1 | -7.4 | 31.1 |
| | $S_1$-2 | 2.9 | 112.1 |

Unit of bond length L is Á, unit of angle is degree (°).

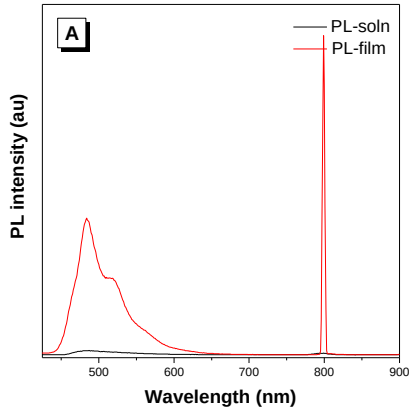


The TICT state is a long-wavelength (800 to 900 nm) energy trap that only exists in the solution state and consumes the excited state energy in a non-radiative form.

**Figure S10.** Photoluminescence (PL) spectra of TZPP in $10^{-3}$ M THF solution and solid film from 425 nm to 900 nm. Related to Figure 2.

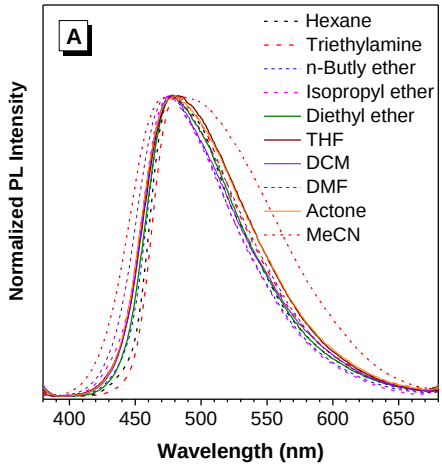


The little change of PL peaks upon increasing solvent polarity indicates the LE characteristic of the emissive state.

**Figure S11.** Photoluminescence (PL) spectra of TZPP in solvents of different polarity. Related to Figure 2.

**Table S3.** Calculated results of absorption and emission properties of TZPP in solid. Related to Figure 2.

| TZPP | | E (eV)/λ (nm) | *f* | P (HOMO->LUMO) |
|---|---|---|---|---|
| Sollid | $S_0$ (Abs.) | 3.61/343 | 0.1520 | 0.96 |
| | $S_1$ (Emission) | 2.88/431 | 0.1030 | 0.97 |

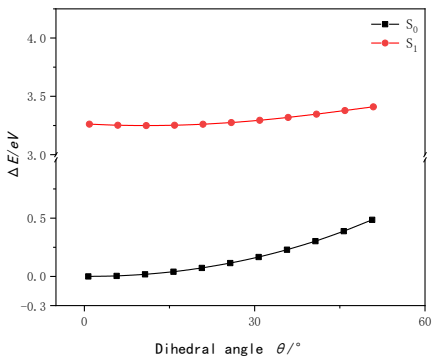


The dihedral angel S1-C6-N3-C7($\theta$) can be only changed from 0 to about 50° due to the restriction from the surrounding molecules.

**Figure S12.** PESs along the central dihedral angle S1–C6–N3–C7 ($\theta$) of TZPP by scanning relaxed geometries in solid. Related to Figure 2.

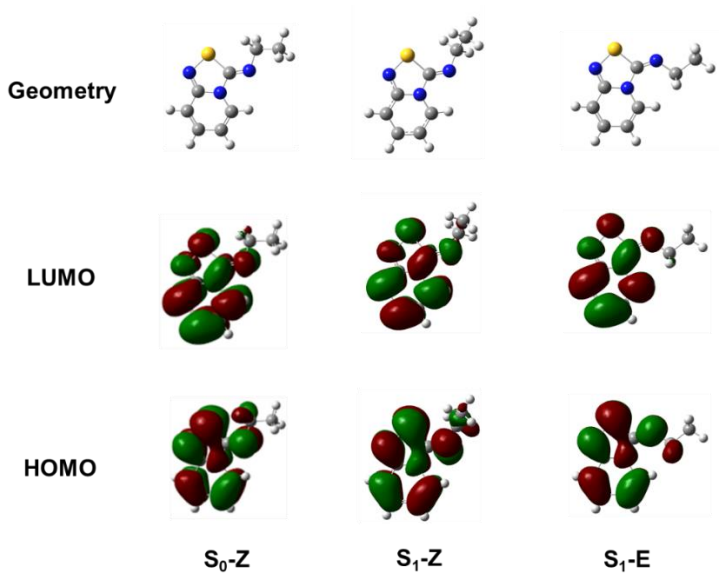


The position change of ethyl group in space has little effect on the $S_0 \rightarrow S_1$ transition of TZPE. The transition characteristic of TZPE should always be LE state stemming from the TZP part.

**Figure S13.** Frontier molecular orbitals of TZPE at $S_0$ and $S_1$. Related to Figure 2.

**Table S4.** Calculated results of absorption and emission properties of TZPE in solution and solid state. Related to Figure 2.

| TZPE | E (eV)/λ (nm) | | *f* | | P (HOMO->LUMO) | |
|---|---|---|---|---|---|---|
| | THF | Solid | THF | Solid | THF | Solid |
| $S_0$ (Abs.) | 3.74/332 | 3.78/328 | 0.1516 | 0.0753 | 0.98 | 0.98 |
| $S_1$ (Emission) | 2.93/422 | 2.94/422 | 0.1206 | 0.0579 | 0.99 | 0.99 |

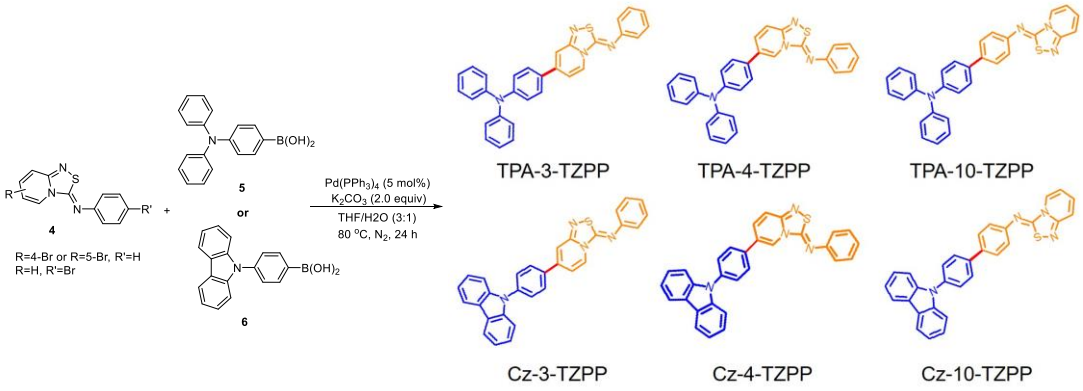


**Figure S14.** Synthetic procedures for TZPP-based derivatives. Related to Figure 3.

Substituted *(Z)-N*-(3*H*-[1,2,4]thiadiazolo[4,3-*a*]pyridin-3-ylidene)-aniline (**4**, 1.0 mmol), (4-(diphenylamino)phenyl)boronic acid (**5**) or (4-(9*H*-carbazol-9-yl)phenyl)boronic acid (**6**, 1.2 mmol), $Pd(PPh_3)_4$ (5 mol %) and $K_2CO_3$ (2.0 mmol) were mixed in THF/$H_2O$ (3:1) to stir under $N_2$ atmosphere at 80 °C. Upon completion, the reaction mixture was washed by saturated NaCl aqueous solution (2×10 mL) and then extracted with dichloromethane (2×10 mL), and the organic layers were combined, dried over anhydrous $MgSO_4$, filtered, and concentrated under reduced pressure. The residue was separated by column chromatography (dichloromethane/hexane = 1: 1) to give the pure yellow products in 86%-95% yields.

**(*Z*)-*N*,*N*-Diphenyl-4-(3-(phenylimino)-3*H*-[1,2,4]thiadiazolo[4,3-*a*]pyridin-7-yl)aniline (TPA-3-TZPP):** yellow solid (86%), mp = 195 - 196 °C; $^1$H NMR (400 MHz, $CDCl_3$) $\delta$ 8.25 (d, *J* = 7.5 Hz, 1H), 7.50 (d, *J* = 8.7 Hz, 2H), 7.43 - 7.39 (m, 2H), 7.34 - 7.30 (m, 4H), 7.21 - 7.09 (m, 12H), 6.77 (dd, *J* = 7.5, 1.2 Hz, 1H); $^{13}$C NMR (100 MHz, $CDCl_3$) $\delta$ 159.0, 149.4, 148.5, 146.9, 145.0, 129.5, 129.1, 127.4, 125.5, 125.2, 124.1, 123.9, 122.2, 121.1, 113.3, 109.7 ppm; $\nu_{max}$(KBr)/cm$^{-1}$ 2918, 2850, 1583, 1480, 1282, 1075, 1016, 750, 685; HRMS-ESI (m/z): calcd for $C_{30}H_{23}N_4S$, $[M+H]^+$: 471.1638, found 471.1637.

**(*Z*)-7-(4-(9*H*-Carbazol-9-yl)phenyl)-*N*-phenyl-3*H*-[1,2,4]thiadiazolo[4,3-*a*]pyridin-3-imine (Cz-3-TZPP):** yellow solid (89%), mp = 190 - 192 °C; $^1$H NMR (400 MHz, $CDCl_3$) $\delta$ 8.34 (d, *J* = 7.5 Hz, 1H), 8.17 (d, *J* = 7.7 Hz, 2H), 7.85 (*d*, J = 8.4 Hz, 2H), 7.72 (d, *J* = 8.4 Hz, 2H), 7.51 - 7.41 (m, 6H), 7.35 -7.31 (m, 3H), 7.21 - 7.16 (m, 3H), 6.85 (dd, *J* = 7.5, 1.4 Hz, 1H); $^{13}$C NMR (100 MHz, $CDCl_3$) $\delta$ 158.8, 151.8, 148.4, 144.8, 140.5, 139.1, 135.6, 129.6, 128.2, 127.4, 126.1, 124.3, 123.7, 121.1, 120.4, 120.4, 115.3, 109.8, 109.7 ppm; $\nu_{max}$(KBr)/cm$^{-1}$ 3052, 2922, 1597, 1525, 1226, 746; HRMS-ESI (m/z): calcd for $C_{30}H_{21}N_4S$, $[M+H]^+$: 469.1481, found 469.1473.

**(*Z*)-*N*,*N*-Diphenyl-4-(3-(phenylimino)-3*H*-[1,2,4]thiadiazolo[4,3-*a*]pyridin-6-yl)aniline (TPA-4-TZPP):** yellow solid (88%), mp = 160- 161 °C;$^1$H NMR (400 MHz, $CDCl_3$) $\delta$ 8.31 (s, 1H), 7.43 (dd, *J* = 9.7, 1.6 Hz, 1H), 7.36 - 7.29 (m, 4H), 7.22 - 7.16 (m, 4H), 7.09 - 7.04 (m, 10H), 7.00 - 6.96 (m, 2H); $^{13}$C NMR (100 MHz, $CDCl_3$) $\delta$ 159.0, 150.7, 148.4, 148.0, 147.3, 134.0, 129.4, 129.3, 128.9, 127.0, 124.6, 124.1, 123.4, 123.4, 123.3, 121.6, 121.0, 119.0 ppm; $\nu_{max}$(KBr)/cm$^{-1}$ 3037, 2923, 1583, 1495, 1325, 1279, 755, 693; HRMS-ESI (m/z): calcd for $C_{30}H_{23}N_4S$, $[M+H]^+$: 471.1683, found 467.1637.

**(*Z*)-6-(4-(9*H*-Carbazol-9-yl)phenyl)-*N*-phenyl-3*H*-[1,2,4]thiadiazolo[4,3-*a*]pyridin-3-imine**

**(Cz-4-TZPP):** yellow solid (95%), mp = 220 - 221 °C; $^{1}$H NMR (400 MHz, $CDCl_3$) *δ* 8.54 (s, 1H), 8.17 (d, *J* = 7.7 Hz, 2H), 7.79 (d, *J* = 8.4 Hz, 2H), 7.68 (d, *J* = 8.4 Hz, 2H), 7.59 (dd, *J* = 9.7, 1.9 Hz, 1H), 7.50 - 7.42 (m, 6H), 7.36 - 7.30 (m, 2H), 7.25 - 7.14 (m, 4H); $^{13}$C NMR (100 MHz, $CDCl_3$) *δ* 158.9, 150.7, 148.3, 140.6, 137.7. 134.6, 133.8, 129.6, 127.7, 127.5, 126.0, 124.4, 123.5, 123.0, 122.8, 121.0, 120.4, 120.2, 119.4, 109.6 ppm; $v_{max}$(KBr)/cm$^{-1}$ 3054, 2921, 1582, 1504, 1444, 1326, 811, 748; HRMS-ESI (m/z): calcd for $C_{30}H_{21}N_4S$, $[M+H]^+$: 469.1481, found 469.1483.

**(*Z*)-4'-((3*H*-[1,2,4]Thiadiazolo[4,3-*a*]pyridin-3-ylidene)amino)-*N*,*N*-diphenyl-[1,1'-biphenyl]-4-amine (TPA-10-TZPP):** yellow solid (86%), mp = 172 - 174 °C; $^{1}$H NMR (400 MHz, $CDCl_3$) *δ* 8.25 (d, *J* = 7.1 Hz, 1H), 7.60 (d, *J* = 8.1 Hz, 2H), 7.49 (d, *J* = 8.2 Hz, 2H), 7.30 - 7.17 (m, 7H), 7.13 (d, *J* = 7.8 Hz, 6H), 7.10 - 6.98 (m, 3H), 6.49 - 6.46 (m, 1H); $^{13}$C NMR (100 MHz, $CDCl_3$) *δ* 158.8, 151.5, 147.1, 147.0, 146.9, 136.4, 134.6, 133.3, 129.2, 127.6, 127.4, 126.1, 124.3, 124.0, 122.8, 121.5, 119.3, 109.7 ppm; $v_{max}$(KBr)/cm$^{-1}$ 3028, 2934, 1593, 1488, 1270, 751; HRMS-ESI (m/z): calcd for $C_{30}H_{23}N_4S$, $[M+H]^+$: 471.1638, found 471.1641.

**(*Z*)-*N*-(4'-(9*H*-Carbazol-9-yl)-[1,1'-biphenyl]-4-yl)-3*H*-[1,2,4]thiadiazolo[4,3-*a*]pyridin-3-imine (Cz-10-TZPP):** yellow solid (93%), mp = 198 - 199 °C; $^{1}$H NMR (400 MHz, $CDCl_3$) *δ* 8.26 (d, *J* = 7.0 Hz, 1H), 8.14 (d, *J* = 7.7 Hz, 2H), 7.80 (d, *J* = 8.0 Hz, 2H), 7.71 (d, *J* = 8.0 Hz, 2H), 7.61 (d, *J* = 7.9 Hz, 2H), 7.51 - 7.37 (m, 4H), 7.30 - 7.27 (m, 4H), 7.22 - 7.14 (m, 1H), 7.07 (d, *J* = 9.3 Hz, 1H), 6.48 - 6.45 (m, 1H); $^{13}$C NMR (100 MHz, $CDCl_3$) *δ* 159.2, 151.5, 147.7, 140.8, 139.7, 136.5, 135.9, 133.3, 128.1, 128.1, 127.3, 126.0, 125.9, 123.4, 121.7, 120.3, 119.9, 119.3, 109.8 ppm; $v_{max}$(KBr)/cm$^{-1}$ 3024, 2924, 1592, 1225, 745; HRMS-ESI (m/z): calcd for $C_{30}H_{20}N_4SNa$, $[M+Na]^+$: 491.1301, found 491.1306.

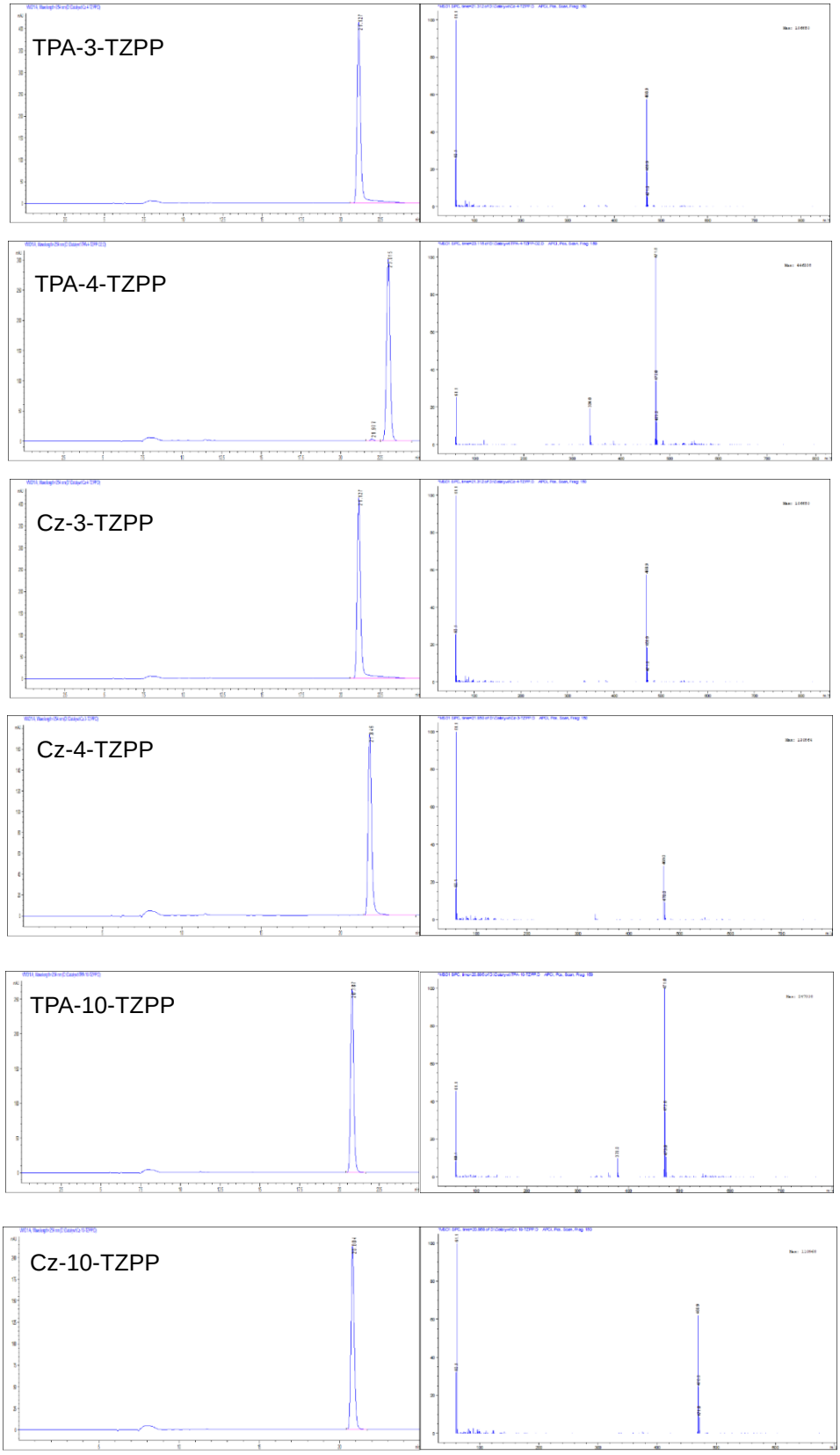


**Figure S15.** TZPP-based derivates were added in water under $O_2$ atmosphere. After 7 days, they were extracted with $CH_2Cl_2$ and then were analyzed with LC-MS. Obvious artifactual bands were not observed. LC-MS of TZPP-based derivates. Related to Figure 3.

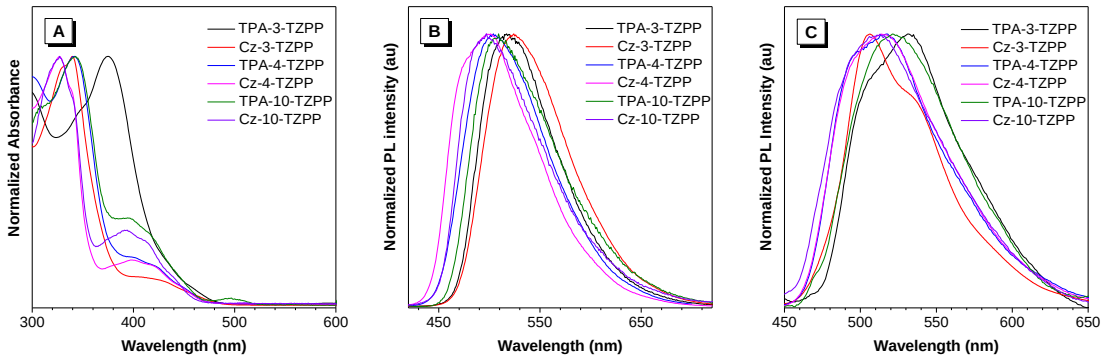


**Figure S16.** (A) Absorption spectra and (B) PL spectra of the TZPP-based derivates in THF solutions; (C) PL spectra of the TZPP-based derivates in solid films state. Related to Figure 4.

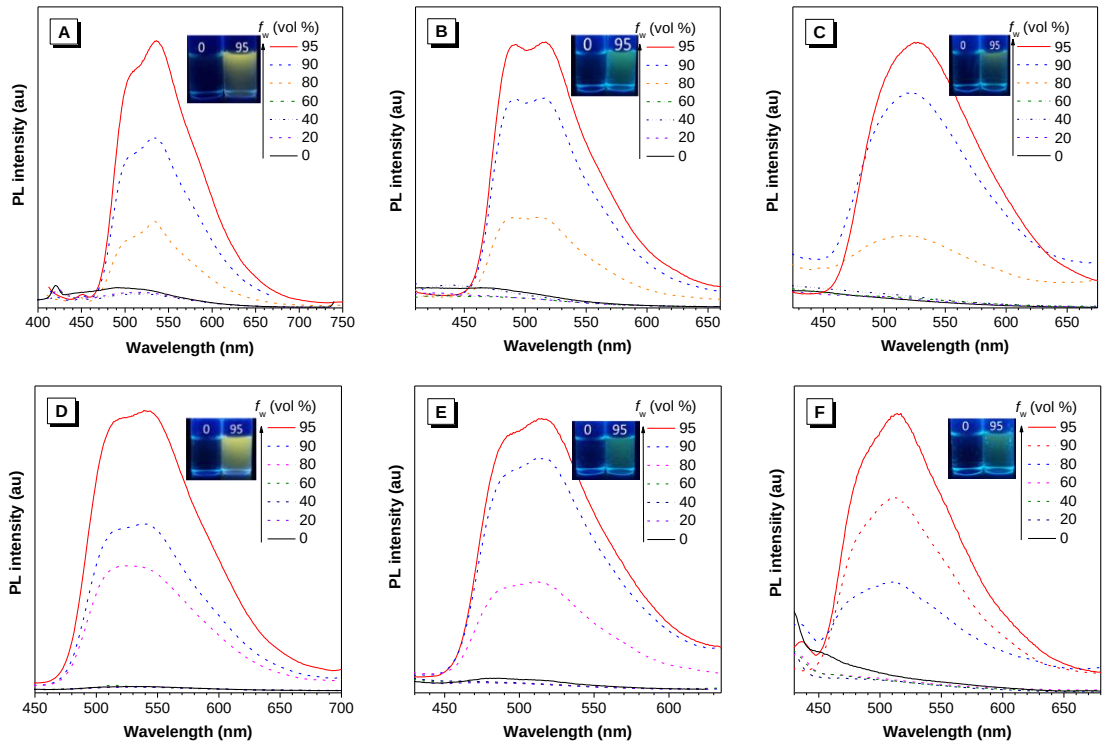


**Figure S17.** PL spectra of (A) TPA-3-TZPP, (B) TPA-4-TZPP, (C) TPA-10-TZPP, (D) Cz-3-TZPP, (E) Cz-4-TZPP, (F) Cz-10-TZPP in THF/water mixtures with different water fractions ($f_w$). Concentration = $10^{-5}$ M. Inset: Photos of the corresponding luminogens in THF-water mixtures ($f_w$ = 0 and 95%), taken under the illumination of a UV lamp (365 nm). Related to Figure 4.

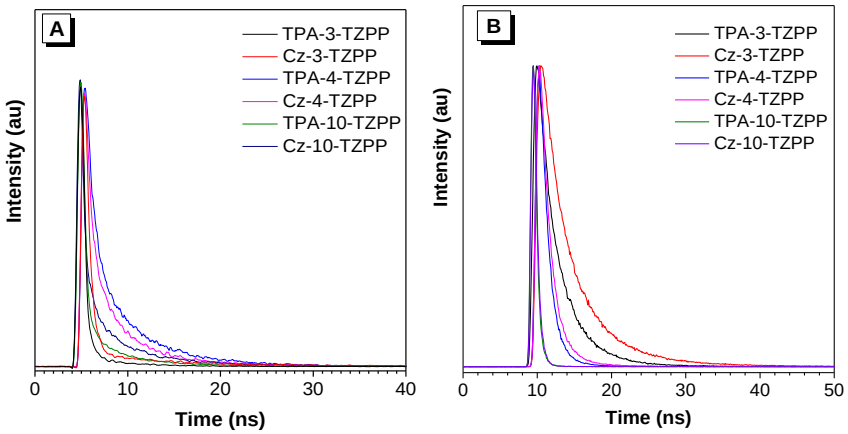


**Figure S18.** Time-resolved fluorescence decay curves of TZPP-based derivatives luminogens: (A) in THF solutions and (B) in solid films. Related to Table 2.

(A) TZPP-based derivates are tested at different temperatures (from 25 °C to 100 °C), and no obvious colour change is observed under the illumination of a UV lamp (365 nm).

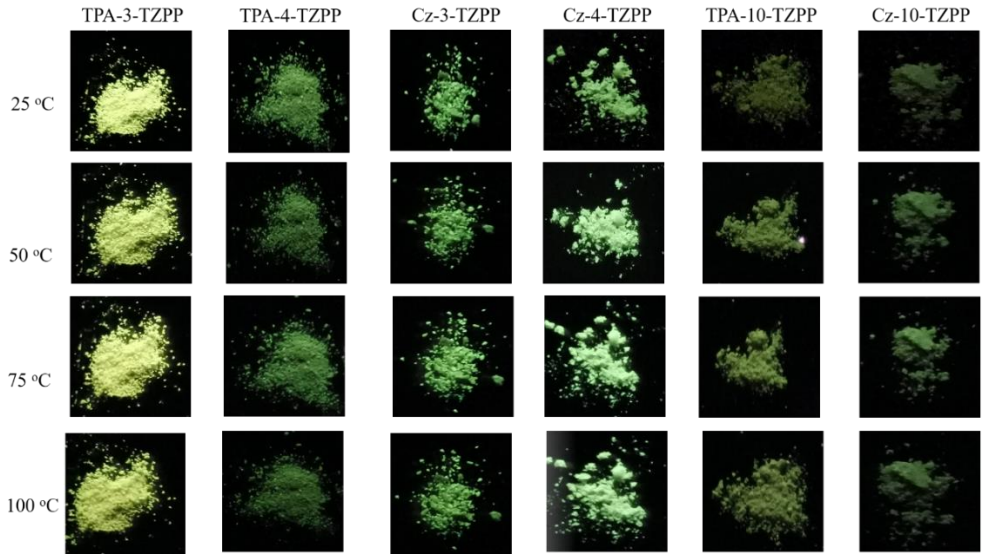


(B) TZPP-based derivates are tested after the 15 minutes vapor of $CH_2Cl_2$, and no obvious colour change is observed under the illumination of a UV lamp (365 nm).

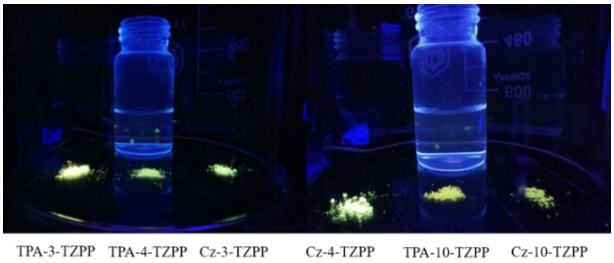


(C) PL spectra of (A) TPA-3-TZPP, (B) TPA-4-TZPP, (C) TPA-10-TZPP, (D) Cz-3-TZPP, (E) Cz-4-TZPP, (F) Cz-10-TZPP in solid state. TZPP-based derivates are tested in pristine and ground state, and no obvious change is observed for the PL spectrum.

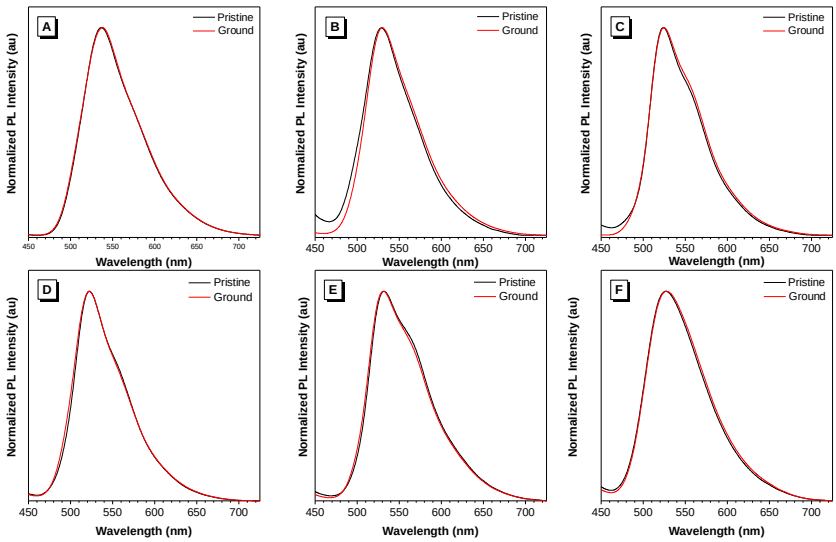


**Figure S19.** External stimuli of TZPP-based derivates about (A) temperature, (B) organic solvent vapors and (C) mechanical force. Related to Figure 4.

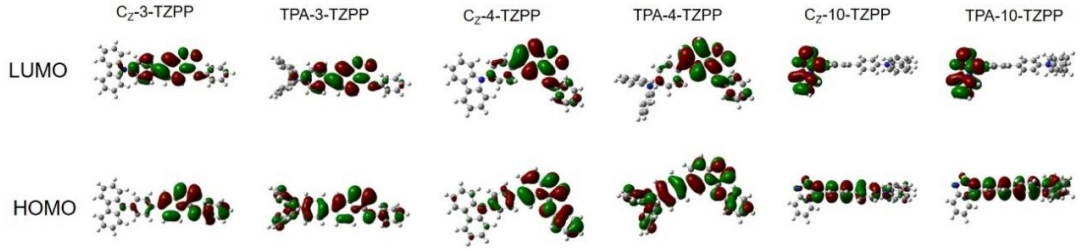


**Figure S20.** Frontier molecular orbitals of TZPP-based derivatives at $S_1$. Related to Table 2.

**Table S5.** Calculated results of absorption and emission properties of TZPP-based derivatives in THF solution. Related to Table 2.

| THF | Abs. | | | Emi. | | |
|---|---|---|---|---|---|---|
| | E (eV)/λ (nm) | *f* | P (HOMO->LUMO) | E (eV)/λ (nm) | *f* | P (HOMO->LUMO) |
| Cz-3-TZPP | 3.44/360 | 0.1225 | 82% | 2.72/456 | 0.1021 | 94% |
| TPA-3-TZPP | 3.44/360 | 0.211 | 58% | 2.75/450 | 0.1559 | 85% |
| Cz-4-TZPP | 3.47/357 | 0.2213 | 79% | 2.76/448 | 0.2022 | 94% |
| TPA-4-TZPP | 3.43/361 | 0.2465 | 59% | 2.79/445 | 0.2187 | 78% |
| Cz-10-TZPP | 3.53/351 | 0.5045 | 66% | 1.48/845 | 0.0026 | 79% |
| TPA-10-TZPP | 3.50/354 | 0.6641 | 56% | 1.42/872 | 0.0012 | 68% |

**X-Ray crystallography**

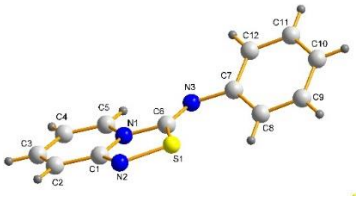


| | |
|---|---|
| Empirical formula | $C_{12}H_9N_3S$ |
| Formula weight | 227.28 |
| Temperature | 100.00 (10) K |
| Wavelength | 1.54184 Å |
| Crystal system, space group | orthorhombic, Pbca |
| Unit cell dimensions | a = 12.8249(3) Å alpha = 90.00 deg.<br>b = 6.97407(14)) Å beta = 90.00 deg.<br>c = 23.3461(5) Å gamma = 90.00 deg. |
| Volume | 2088.12(8) $Å^3$ |
| Z, Calculated density | 8, 1.446 $Mg/m^3$ |
| Absorption coefficient | 2.519 $mm^{-1}$ |
| F(000) | 944.0 |
| Crystal size | 0.2 × 0.16 × 0.12 $mm^3$ |
| 2Θ range for data collection | 7.574 to 147 deg. |
| Limiting indices | $-14 \leq h \leq 15$, $-5 \leq k \leq 8$, $-28 \leq l \leq 25$ |
| Reflections collected / unique | 4729 / 2065, [R(int) = 0.0225] |
| Refinement method | Full-matrix least-squares on $F^2$ |
| Data / restraints / parameters | 2065 / 0 / 146 |
| Goodness-of-fit on $F^2$ | 1.012 |
| Final R indices [I>2sigma(I)] | $R_1$ = 0.0393, $wR_2$ = 0.1111 |
| R indices (all data) | $R_1$ = 0.0403, $wR_2$ = 0.1124 |

**Figure S21.** ORTEP drawings of TZPP. Thermal ellipsoids are scaled to the 50% probability level. Crystal data have been deposited to CCDC, number 1921846. Related to Scheme 2.

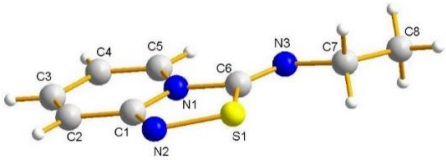


| | |
|---|---|
| Empirical formula | $C_8H_9N_3S$ |
| Formula weight | 179.24 |
| Temperature | 100.00 (10) K |
| Wavelength | 0.71073 Å |
| Crystal system, space group | monoclinic, $P2_1/n$ |
| Unit cell dimensions | a = 3.9658(3) Å alpha = 90.00 deg.<br>b = 17.1192(13)) Å beta = 92.913(8) deg.<br>c = 12.3386(11) Å gamma = 90.00 deg. |
| Volume | 836.60(12) $Å^3$ |
| Z, Calculated density | 4, 1.423 $Mg/m^3$ |
| Absorption coefficient | 0.329 $mm^{-1}$ |
| F(000) | 376.0 |
| Crystal size | 0.21×0.15×0.12 $mm^3$ |
| Theta range for data collection | 3.514 to 29.593 deg. |
| Limiting indices | $-4 \leq h \leq 5$, $-23 \leq k \leq 21$, $-16 \leq l \leq 15$ |
| Reflections collected / unique | 6675 / 2060, [R(int) = 0.0294] |
| Refinement method | Full-matrix least-squares on $F^2$ |
| Data / restraints / parameters | 2060 / 0 / 110 |
| Goodness-of-fit on $F^2$ | 1.090 |
| Final R indices [I>2sigma(I)] | $R_1$ = 0.0421, $wR_2$ = 0.0893 |
| R indices (all data) | $R_1$ = 0.0507, $wR_2$ = 0.0932 |

**Figure S22.** ORTEP drawings and packing diagrams of TZPE. Thermal ellipsoids are scaled to the 50% probability level. Crystal data have been deposited to CCDC, number 1588922. Related to Scheme 2.

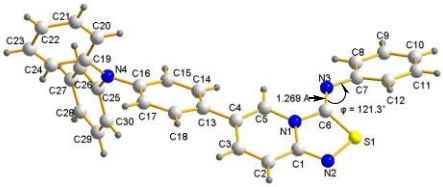


| | |
|---|---|
| Empirical formula | $C_{30}H_{22}N_4S$ |
| Formula weight | 470.57 |
| Temperature | 100.00 (10) K |
| Wavelength | 1.54184 Å |
| Crystal system, space group | monoclinic, $P2_1/n$ |
| Unit cell dimensions | a = 15.6836(12) Å alpha = 90.00 deg.<br>b = 10.1472(6) Å beta = 116.678(9) deg.<br>16.4808(12) Å gamma = 90.00 deg. |
| Volume | 2343.6(3) $Å^3$ |
| Z, Calculated density | 4, 1.334 $Mg/m^3$ |
| Absorption coefficient | 1.429 $mm^{-1}$ |
| F(000) | 984.0 |
| Crystal size | 0.21 × 0.16 × 0.11 $mm^3$ |
| 2Θ range for data collection | 10.488 to 147.374 deg. |
| Limiting indices | -19 ≤ h ≤ 18, -12 ≤ k ≤ 7, -20 ≤ l ≤ 19 |
| Reflections collected / unique | 8571 / 4567, [R(int) = 0.0341] |
| Refinement method | Full-matrix least-squares on $F^2$ |
| Data / restraints / parameters | 4567 /0 / 316 |
| Goodness-of-fit on $F^2$ | 1.065 |
| Final R indices [I>2sigma(I)] | $R_1$ = 0.0667, $wR_2$ = 0.1717 |
| R indices (all data) | $R_1$ = 0.0738, $wR_2$ = 0.1790 |

**Figure S23.** ORTEP drawings of TPA-4-TZPP. Thermal ellipsoids are scaled to the 50% probability level. Crystal data have been deposited to CCDC, number 1921837. Related to Figure 3.

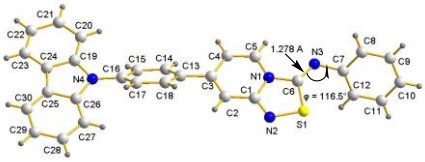


| | |
|---|---|
| Empirical formula | $C_{30}H_{20}N_4S$ |
| Formula weight | 468.56 |
| Temperature | 100.00 (10) K |
| Wavelength | 0.71073 Å |
| Crystal system, space group | triclinic, P-1 |
| Unit cell dimensions | a = 10.5182(7) Å alpha = 100.757(7) deg.<br>b = 10.7393(10) Å beta = 95.409(6) deg.<br>c = 11.6358(8) Å gamma =117.359(8) deg. |
| Volume | 1122.15(17) $Å^3$ |
| Z, Calculated density | 2, 1.387 $Mg/m^3$ |
| Absorption coefficient | 0.173 $mm^{-1}$ |
| F(000) | 488.0 |
| Crystal size | 0.14×0.12×0.10 $mm^3$ |
| 2Θ range for data collection | 7.286 to 58.908 deg. |
| Limiting indices | -13≤ h ≤ 10, -12≤ k ≤ 14, -12 ≤ l ≤ 14 |
| Reflections collected / unique | 6220 / 5234, [R(int) = 0.0214] |
| Refinement method | Full-matrix least-squares on $F^2$ |
| Data / restraints / parameters | 5234 / 0 / 316 |
| Goodness-of-fit on $F^2$ | 0.998 |
| Final R indices [I>2sigma(I)] | $R_1$ = 0.0463, $wR_2$ = 0.1100 |
| R indices (all data) | $R_1$ = 0.0580, $wR_2$ = 0.1195 |

**Figure S24.** ORTEP drawings of Cz-3-TZPP. Thermal ellipsoids are scaled to the 50% probability level. Crystal data have been deposited to CCDC, number 1921840. Related to Figure 3.

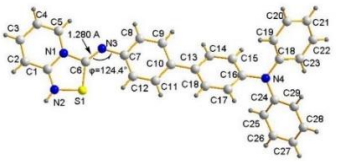


| | |
|---|---|
| Empirical formula | $C_{30}H_{22}N_4S$ |
| Formula weight | 470.57 |
| Temperature | 293.02(10) |
| Wavelength | 1.54184 Å |
| Crystal system, space group | monoclinic, $P2_1/c$ |
| Unit cell dimensions | a = 7.4313(2) Å alpha = 90 deg.<br>b = 38.9483(10) Å beta = 100.636(3) deg.<br>c = 8.2436(3) Å gamma = 90 deg. |
| Volume | 2345.01(12) $Å^3$ |
| Z, Calculated density | 2, 1.333 $Mg/m^3$ |
| Absorption coefficient | 1.428 $mm^{-1}$ |
| F(000) | 984.0 |
| Crystal size | 0.12 × 0.11 × 0.1 $mm^3$ |
| 2Θ range for data collection | 4.538 to 147.942 deg. |
| Limiting indices | $-8 \le h \le 5$, $-48 \le k \le 46$, $-10 \le l \le 10$ |
| Reflections collected / unique | 8913/4595, [R(int) = 0.0265] |
| Refinement method | Full-matrix least-squares on $F^2$ |
| Data / restraints / parameters | 4595/ 0/ 316 |
| Goodness-of-fit on $F^2$ | 1.054 |
| Final R indices [I>2sigma(I)] | $R_1$ = 0.0372, $wR_2$ = 0.0873 |
| R indices (all data) | $R_1$ = 0.0422, $wR_2$ = 0.0907 |

**Figure S25.** ORTEP drawings of TPA-10-TZPP. Thermal ellipsoids are scaled to the 50% probability level. Crystal data have been deposited to CCDC, number 1921842. Related to Figure 3.

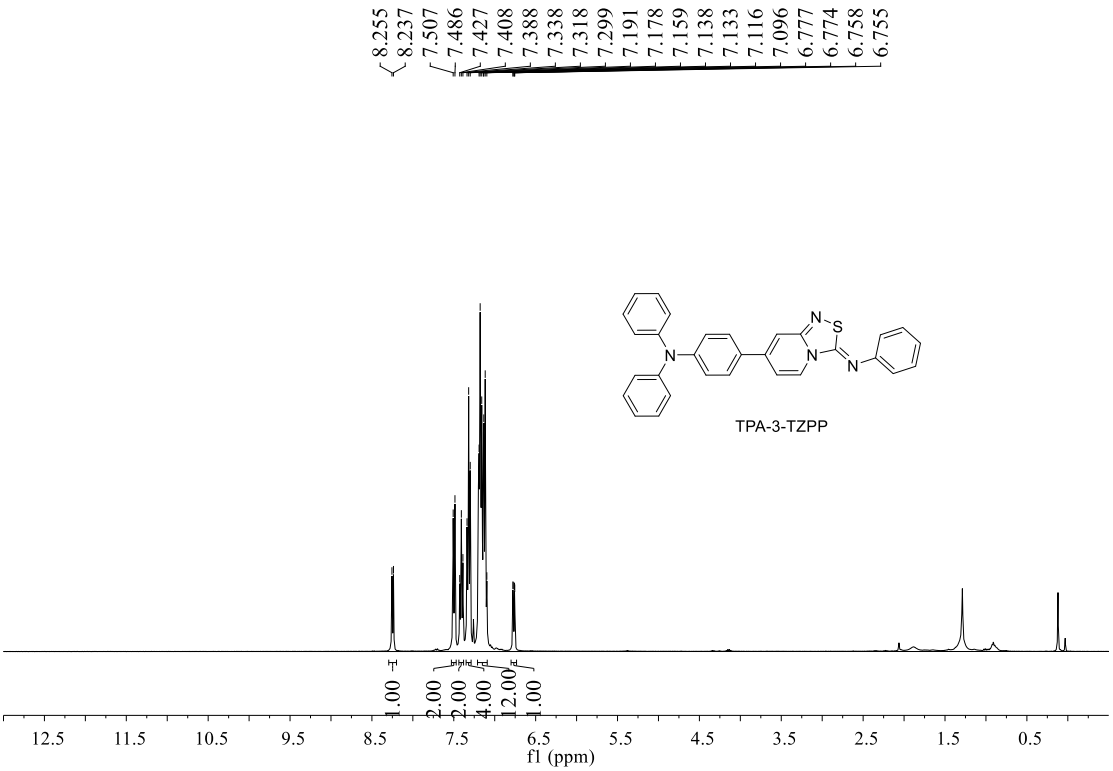


**Figure S26.** $^{1}$H NMR of TPA-3-TZPP in $CDCl_3$. Related to Figure 3.

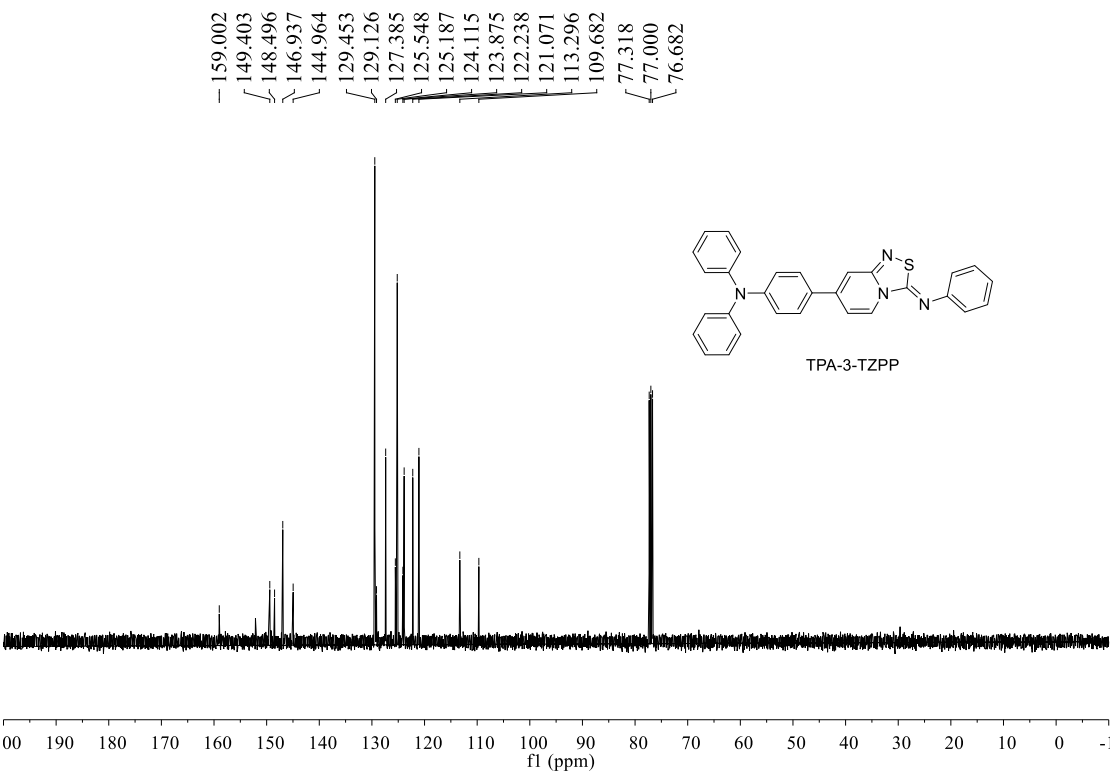


**Figure S27.** $^{13}$C NMR of TPA-3-TZPP in $CDCl_3$. Related to Figure 3.

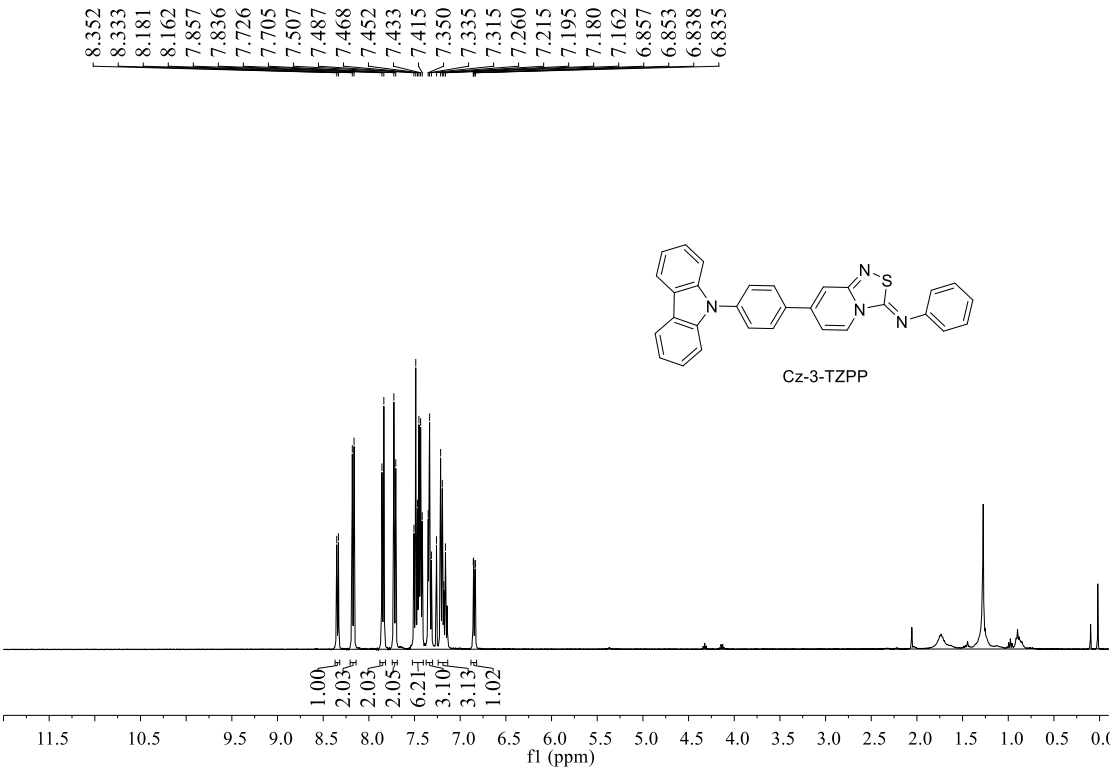


**Figure S28.** $^{1}$H NMR of Cz-3-TZPP in $CDCl_3$. Related to Figure 3.

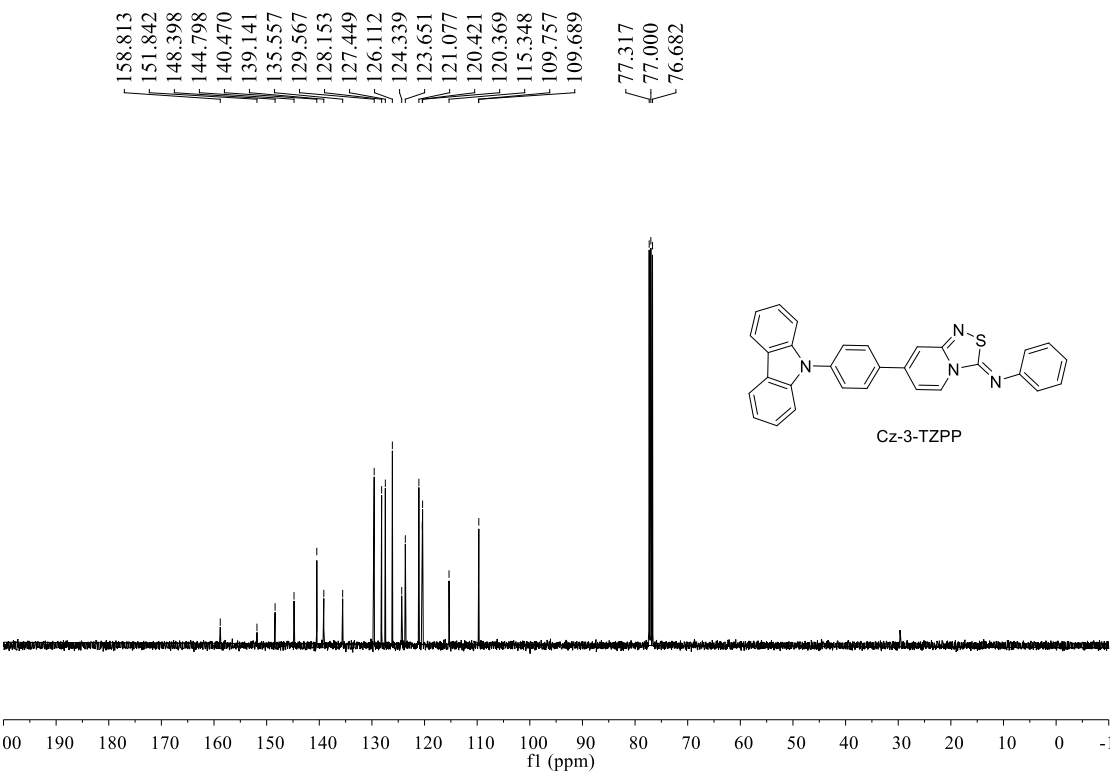


**Figure S29.** $^{13}$C NMR of Cz-3-TZPP in $CDCl_3$. Related to Figure 3.

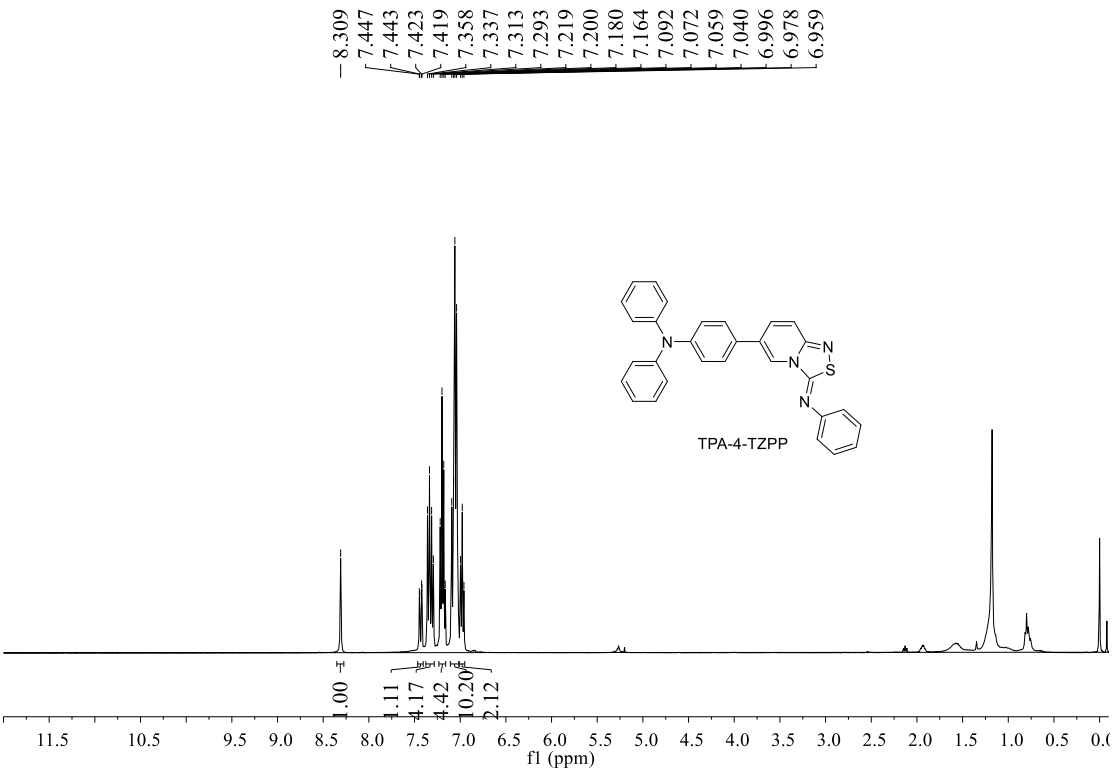


**Figure S30.** $^{1}$H NMR of TPA-4-TZPP in $CDCl_3$. Related to Figure 3.

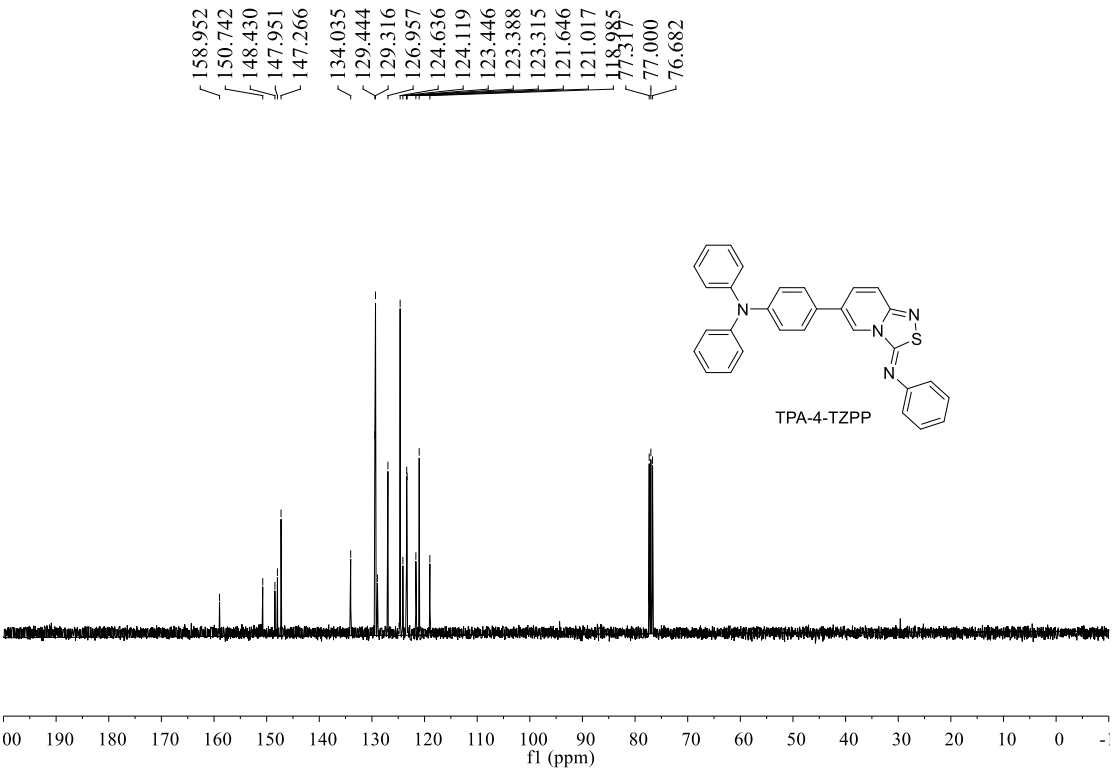


**Figure S31.** $^{13}$C NMR of TPA-4-TZPP in $CDCl_3$. Related to Figure 3.

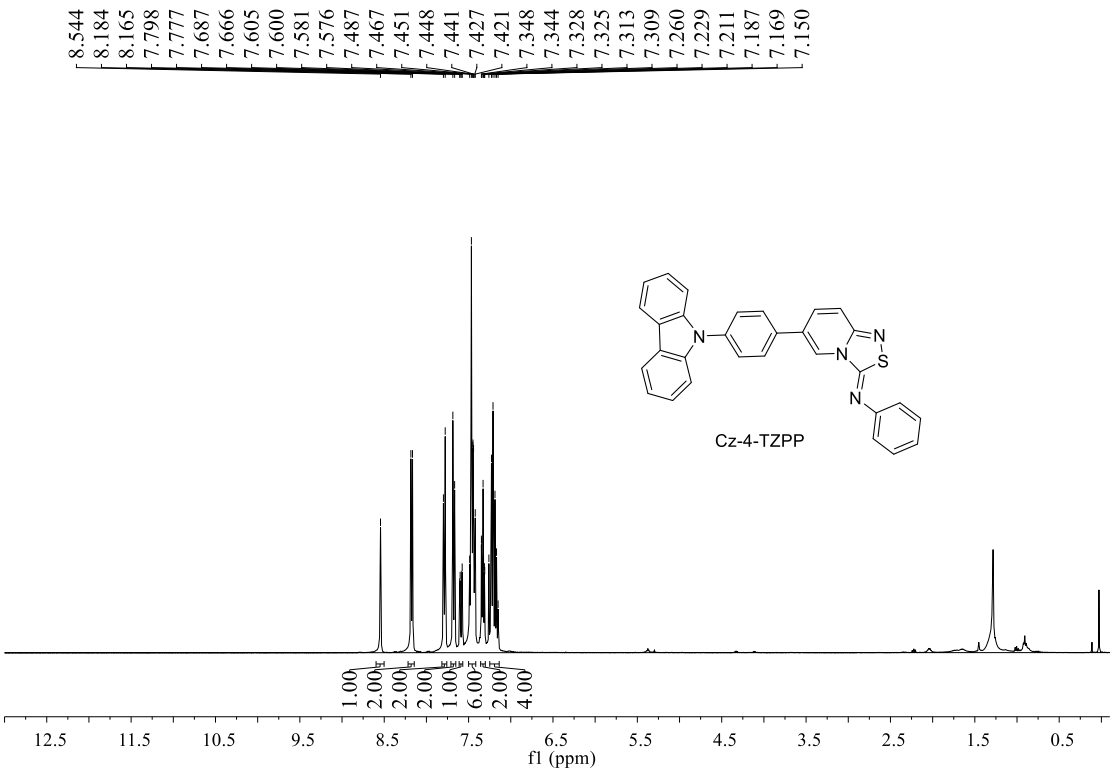


**Figure S32.** $^{1}$H NMR of Cz-4-TZPP in $CDCl_3$. Related to Figure 3.

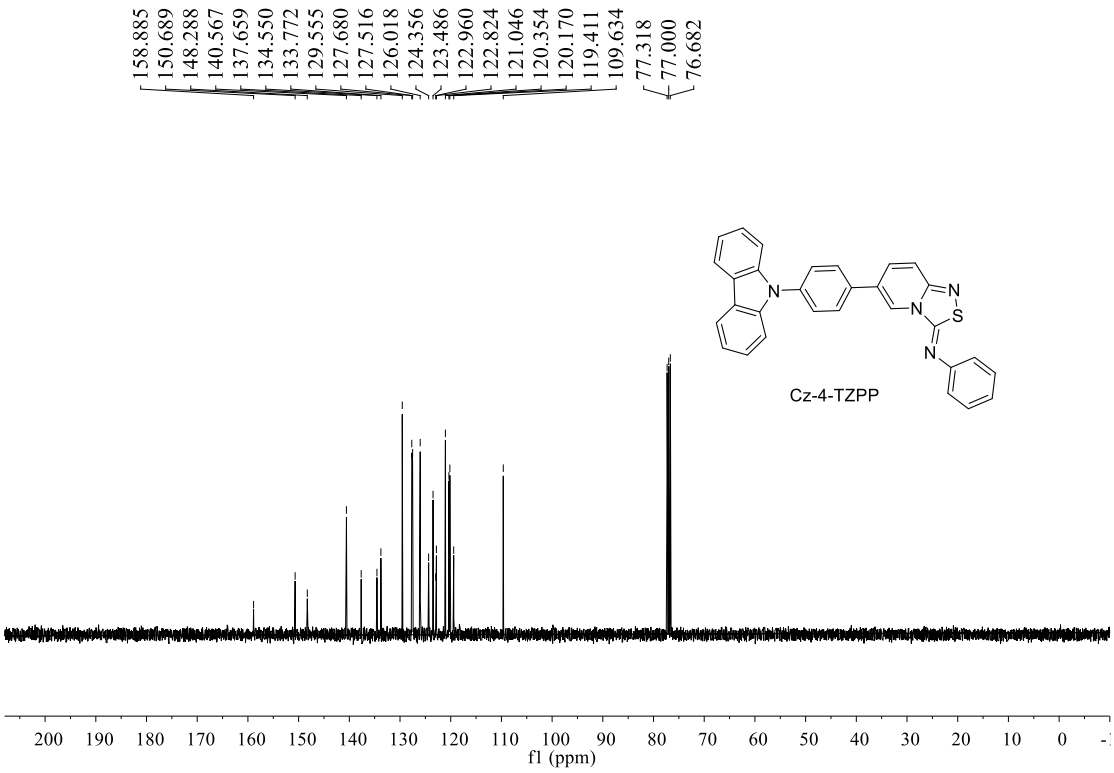


**Figure S33.** $^{13}$C NMR of Cz-4-TZPP in $CDCl_3$. Related to Figure 3.

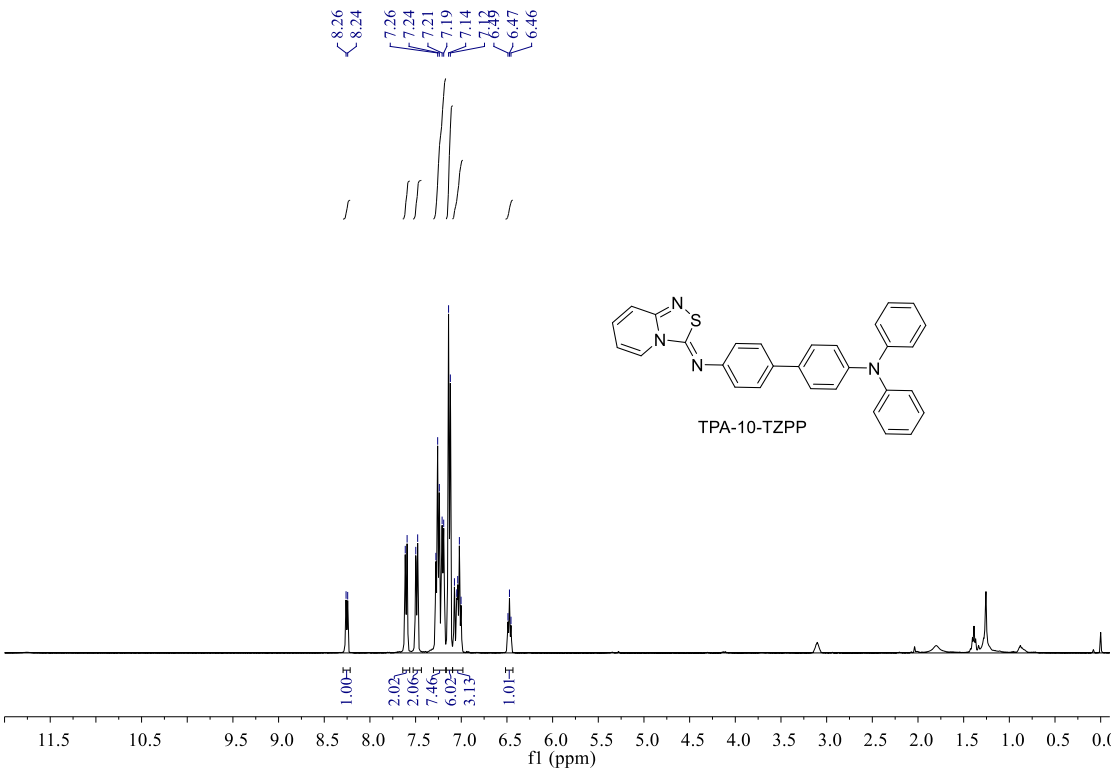


**Figure S34.** $^{1}$H NMR of TPA-10-TZPP in $CDCl_3$. Related to Figure 3.

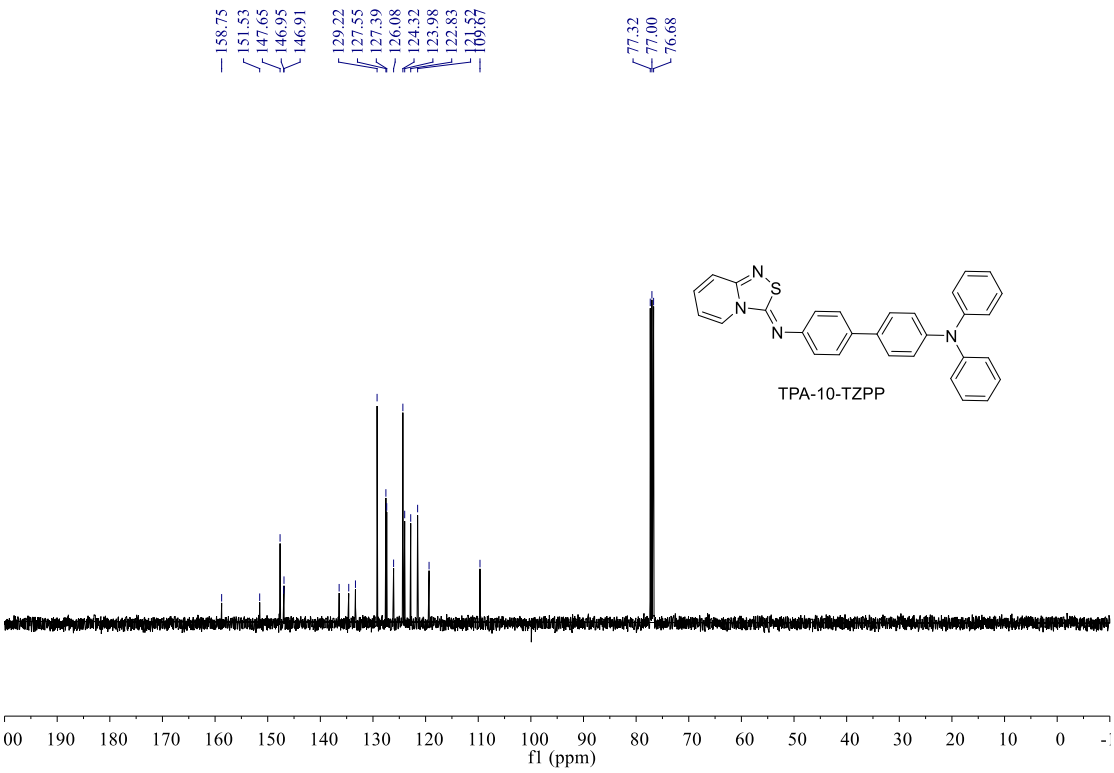


**Figure S35.** $^{13}$C NMR of TPA-10-TZPP in $CDCl_3$. Related to Figure 3.

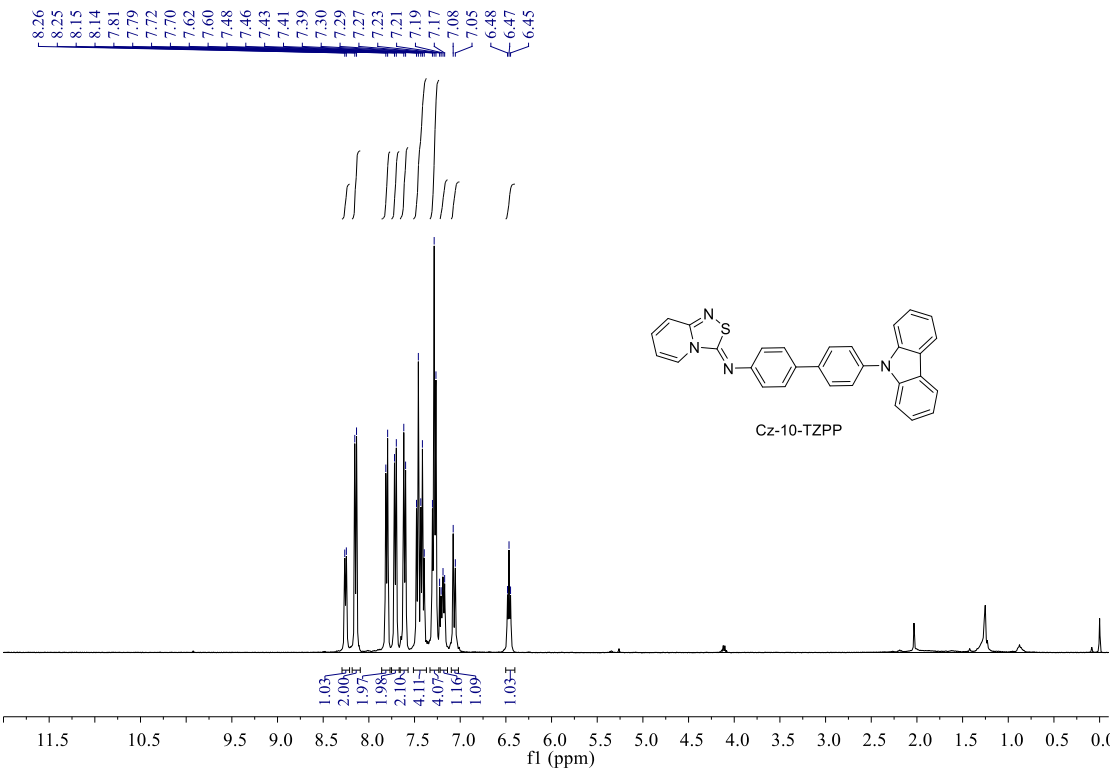


**Figure S36.** $^{1}$H NMR of Cz-10-TZPP in $CDCl_3$. Related to Figure 3.

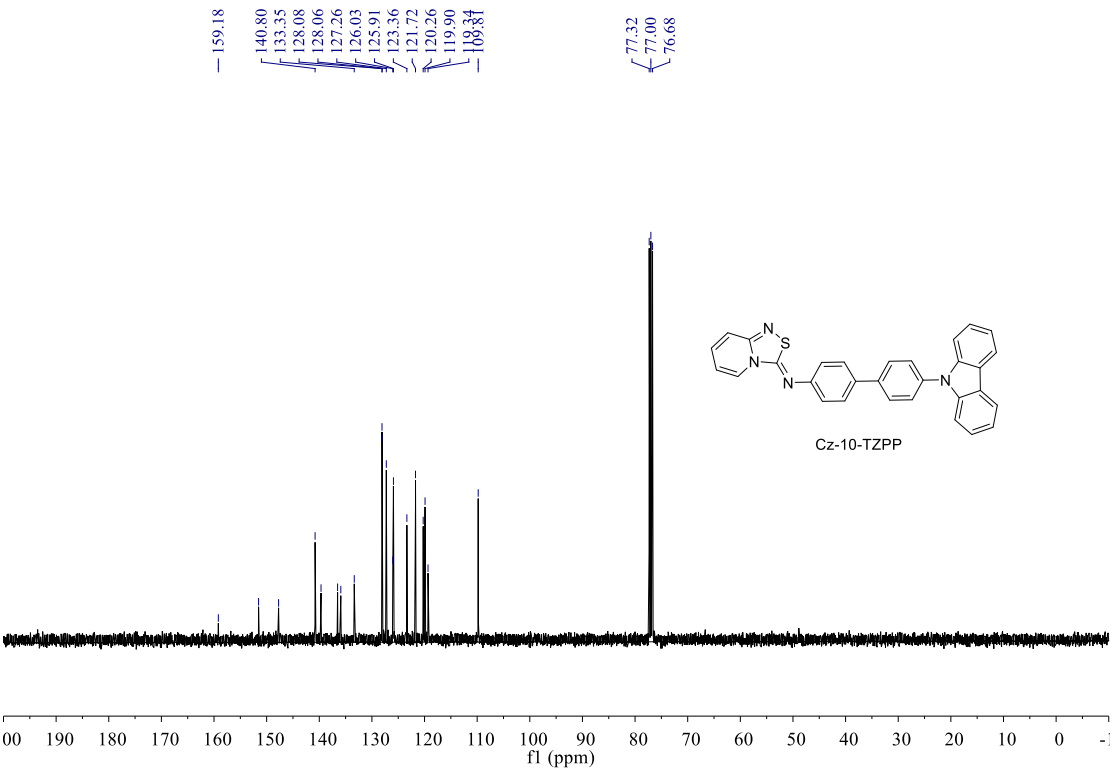


**Figure S37.** $^{13}$C NMR of Cz-10-TZPP in $CDCl_3$. Related to Figure 3.